A Multiscale Study of MOFs as Adsorbents in H2 PSA Purification

A multi-scale study of MOFs as adsorbents in H_2 PSA purification

*Ana-Maria Banu, Daniel Friedrich, Stefano Brandani, Tina Düren**

Institute for Materials and Processes, School of Engineering, The University of Edinburgh,

Sanderson Building, The King's Buildings, Mayfield Road

Edinburgh, EH9 3JL, UK

tina.duren@ed.ac.uk

Abstract

In this multi-scale study, four robust, zirconium oxide based metal organic frameworks (MOFs), were examined using powerful molecular simulation tools as well as indispensable full-scale PSA system modeling in order to determine their potential for H_2 purification. Grand canonical Monte Carlo (GCMC) and molecular dynamics (MD) simulations were employed in order to evaluate the MOF working capacities, binary mixture selectivities, and micropore transport diffusivities for each of the components of a steam methane reformer offgas (SMROG) stream: H_2, CO, CH_4, N_2 and CO_2. The small, functionalized pores of UiO-66(Zr)-Br were found to result in high N_2 and CO selectivities and working capacities, while the slightly larger pore volume of UiO-66(Zr) favored higher CO_2 and CH_4 working capacities. The collective

impact of impurity uptakes and selectivities on the purification of H_2 from five-component steam methane reformer offgas mixtures was investigated through PSA column modeling. The breakthrough behavior of SMROG mixtures in columns containing MOF crystallites was determined using the simulated adsorption and diffusivity data as input. MOF breakthrough curves for single as well as two layered beds, were compared to those of commercial adsorbents including Zeolite 5A and Calgon PCB. Two of the MOFs, namely UiO-66(Zr) and UiO-66(Zr)-Br were found to have longer dimensionless breakthrough times than the commercial zeolite materials, and are therefore expected to result in larger yields of high purity H_2 per PSA cycle. UiO-66(Zr)-Br was found to be the most promising of the four MOFs, having the longest dimensionless breakthrough times in both, single and two-layered bed setups.

Keywords Pressure swing adsorption, metal-organic frameworks, gas separation, hydrogen purification, molecular simulations, breakthrough curves, adsorption, diffusion.

1. Introduction

Pressure swing adsorption (PSA) units[1-4] are the technology of choice in hydrogen purification, accounting for 85% of the world's hydrogen production. In a hydrogen PSA unit, gas streams are separated mainly based on equilibrium selectivity, i.e. the relative adsorption strengths of the components, which is determined by molecular volatility and polarity. One of the most common feed streams used in hydrogen PSA systems is steam methane reformer offgas (SMROG), which normally has a H_2 content of 70-80%.[3] The remainder of the mixture is composed of CO_2, CH_4 (and higher hydrocarbons), CO, and N_2, which must be removed in order to produce high purity H_2.

PSA units require high-performance adsorbents that have large capacities and selectivities for the impurities to be removed, and which can be easily regenerated at low pressure.[3] Feed streams generally enter a PSA process at 4 – 30 atm, while the waste streams containing desorbed impurities leave the columns at 1.1 – 1.7 atm.[3] Depending on the process temperature and pressure, frequently utilized adsorbents include activated aluminas, silica gels, activated carbons (ACs) and zeolites. Activated carbons are beneficial for the removal of CO_2 and hydrocarbons due to their high capacities and low adsorption enthalpies, however their non-polar structures and large pore diameters render them less advantageous in the removal of N_2 and CO. Zeolites on the other hand, have high selectivities for the polar adsorbates, but are difficult to regenerate upon CO_2 adsorption due to the high interaction strength between the CO_2 molecules and the charged zeolite pore surface. In order to increase separation efficiency, adsorption columns often contain two or more adsorbent layers, each of which is designed to target specific impurities.[5-9] Such columns allow for CO_2 to be retained in easily regenerated activated carbon particles, while lighter impurities are adsorbed in highly selective zeolite layers. The overall performance of the

PSA unit is highly dependent on the adsorbents chosen and is limited by the selectivity of the adsorbent for the most weakly interacting impurity – N_2 in the case of SMROG. Once this impurity breaks through the adsorption column, the feed cycle must be stopped and the adsorbent must be regenerated.

In the continuous search for high-performance adsorbent materials required in order to improve PSA product yield, purity and energy requirements, metal-organic frameworks (MOFs) have been identified as promising candidates. While many MOF studies have focused on adsorption of binary, and ternary mixtures[10] containing the more abundant impurities, that is CO_2 and CH_4, only a few have analyzed CO/H_2 and N_2/H_2 mixture adsorption. It is important to bear in mind that PSA performance is determined by the adsorption behavior of each of the impurities, and that adsorption strength can vary widely depending on the polarity of the impurity and on the properties of the MOF such as pore size, topology and chemical functionality. Furthermore, the impurities are competing with each other for the adsorption sites available, therefore in order to identify the most promising MOFs for H_2 purification a study of the adsorption as well as the micropore and macropore diffusion behavior of the complete mixture is required. A study of diffusion through the micropores is necessary in order to verify the dominant mass transfer resistance.

According to the detailed report of Sircar and Golden, the criteria by which PSA adsorbents should be selected include multicomponent adsorption capacities, desorption behavior, selectivities and isosteric heats of adsorption.[11] None of these factors however, can be used as a single selection criterion, as separation efficiency is affected by each parameter to some degree.[12-14]

The most effective method for testing the selective properties of materials to be used in separating H_2 from multicomponent mixtures is the use of laboratory scale breakthrough and PSA cycle experiments, such as the Dual Piston PSA setup[15], as well as mathematical models, which simulate column adsorption. As a result, numerous zeolite and activated carbon studies seeking to identify promising PSA adsorbents have presented breakthrough studies and PSA process modeling for multicomponent H_2 mixtures through single as well as layered beds.[9, 16-20] Recently, breakthrough models have been employed to investigate whether MOFs can be used in PSA separations for various applications with mixtures containing up to four gases. A study carried out by Krishna and Long compared several MOFs to zeolites and activated carbons using breakthrough studies of $CO_2/CH_4/H_2$ mixtures as well as binary combinations of the three gases.[12] Their work highlighted the advantage of using breakthrough calculations for separation studies, and showed that Mg MOF-74 was the best material for CO_2/H_2, CO_2/CH_4 and CH_4/H_2 separations.[12] Herm et al. investigated CO_2/CH_4, CH_4/H_2 and $CO_2/CH_4/H_2$ separations, processes which are relevant for CO_2 capture and storage as well as for H_2 purification, and found Mg MOF-74 to outperform Zeolite 13X for all three mixtures.[21] Finally, the recent work of Wu et al. tested the performance of MOFs and zeolites in separating $CO_2/CO/CH_4/H_2$, CO_2/H_2, CH_4/H_2 and CO_2/CH_4 mixtures, and identified Cu-TDPAT as a particularly effective adsorbent for H_2 PSA purification from SMROG.[22]

A typical SMROG stream to be introduced into a hydrogen purification PSA unit contains H_2, N_2, CO, CH_4, CO_2. Water is also normally present; however it is the most strongly adsorbed component and can be easily removed from the stream either prior to the PSA unit, or by using additional adsorbent layers in the PSA column. In this study the stream entering the PSA column is assumed to be water-free. Considering the wide variation in selectivities not only from one

MOF to another but also from one impurity to another, it is critical to include all mixture components in the modeling of breakthrough curves. In this work, we use a combination of powerful simulation tools in order to perform a multi-scale study on the progression of five-component mixtures, consisting of both, weakly interacting gases such as N_2 and CO as well as easily adsorbed gases such as CH_4 and CO_2, through columns containing four MOFs. While PSA studies in the literature are normally carried out, at least partially through experimental work, we present an entirely computational study enabled by a transition from simulations at the molecular level, to simulations performed on the unit operations scale. To the best of our knowledge this is the first time such a study, focusing on H_2 purification from SMROG, has been published.

The adsorption and diffusion of five-component mixtures in four MOFs, namely dehydroxylated UiO-66(Zr), UiO-66(Zr)-Br, UiO-67(Zr) and Zr-Cl_2AzoBDC, which share the same topology as shown in Figure 1, was assessed in order to evaluate their potential for hydrogen purification. The MOFs were selected for their stability and resistance to solvents and mechanical pressure.[23, 24] In addition, the water stability studies of Yang et al.[25] and Biwas et al.[26] have shown that the four MOFs retain their crystallinity upon immersion in water. The high connectivity of metal centres to organic linkers, which is characteristic of the UiO-66 family, results in high shear and bulk moduli and is responsible for the excellent mechanical stability of these materials.[24] The structures share the same inorganic zirconium oxide clusters, however the organic linkers connecting the metal clusters vary as shown in **Figure 1**, resulting in different pore sizes, pore volumes, and adsorption site strength. In the first part of the study, results from grand canonical Monte Carlo (GCMC) simulations are presented to determine the working capacities and selectivities for each of the impurities to be removed. With the help of external force non-equilibrium molecular dynamics (EF-NEMD) simulations micropore transport

diffusivities of the mixture components in each of the four MOFs were calculated. The adsorption and diffusion data obtained through molecular simulations were then directly introduced as input into a PSA unit model.

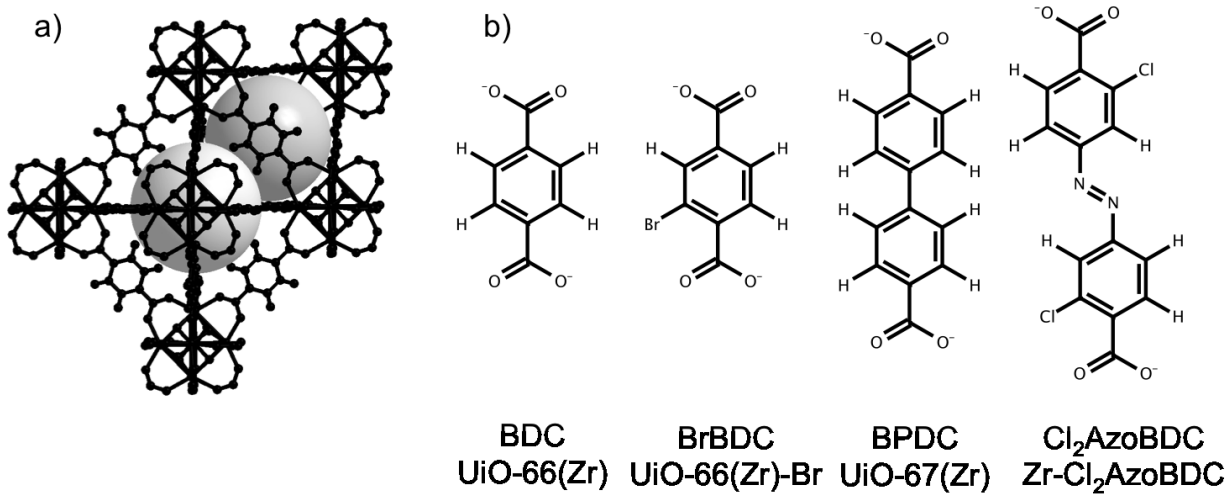

Figure 1. a) Octahedral and tetrahedral pores of UiO-66(Zr) b) Linkers joining the zirconium clusters in each of the four MOFs

In the second part of our work, we employed an adsorption column model in order to study mixture adsorption and diffusion through adsorption columns containing each of the four MOFs alone or containing a layered bed consisting of activated carbon and a MOF. The breakthrough curves for each of the mixture components were analyzed, and the impact of the impurities on the overall performance of different MOFs for hydrogen purification from SMROG is discussed. The breakthrough study was extended to include the zeolite and activated carbon materials studied in detail by Rodrigues and co-workers[16, 27] as well as Zeolite 5A and Calgon PCB[17, 28] in order to determine whether MOFs are able to compete with commercial PSA adsorbents, and to identify which of the four MOFs is the most promising adsorbent for H_2 PSA purification.

2. Methods

2.1. GCMC Simulations

Grand canonical Monte Carlo simulations were carried out using the multipurpose simulation code (MuSiC)[29] in order to determine the adsorption isotherms of each of the pure gases as well as the binary mixtures at 298 K. Each MOF was treated as a rigid structure and the framework atoms were maintained fixed at their crystallographic positions.[23, 25, 26, 30] The simulated adsorbate-adsorbate and adsorbate-framework interactions included both dispersion and electrostatic contributions. Dispersion, or van der Waals interactions, were modeled using the Lennard-Jones potential[31] with a 12.8 Å cut-off, while the electrostatic interactions were calculated using the Ewald summation method.[32] Periodic boundary conditions were applied in order to mimic an infinite crystal structure. The Lennard Jones parameters used to represent framework atoms were taken from the Universal Force Field (UFF),[33] and the partial charges were adopted from previous studies.[25, 30, 34] CH_4, N_2 and CO_2 were modeled using the LJ parameters and partial charges given in the TraPPE force field.[35, 36] CO was described using the model of Martín-Calvo et al.[37], while for H_2 the two-site model of Yang was adopted.[38] Potential parameters between unlike adsorbate-adsorbate and adsorbate-adsorbent atom pairs were determined using the Lorentz-Berthelot mixing rules. The Peng-Robinson[39] equation of state with quadratic mixing rules was applied in order to determine the gas-phase fugacities for pure adsorbates as well as mixtures.

The differential enthalpy of adsorption, was calculated directly from GCMC simulations as follows:[40]

$$\Delta h = \mathrm{R}T - \frac{\langle U_{ads} N_{ads} \rangle - \langle U_{ads} \rangle \langle N_{ads} \rangle}{\langle N_{ads}^2 \rangle - \langle N_{ads} \rangle \langle N_{ads} \rangle} \qquad (1)$$

Here Δh denotes the differential enthalpy of adsorption, R is the universal gas constant, T is the simulation temperature, $<U_{ads}>$ is the average potential energy per molecule, and $<N_{ads}>$ is the average number of molecules adsorbed. The pore diameters were evaluated using the pore size distribution method of Gelb and Gubbins[41] which give the diameter of the largest sphere that can be inserted without overlapping with any of the framework atoms. The pore volumes were determined using a numerical Monte Carlo algorithm to carry out random trial insertions using a 0 Å probe molecule. This purely geometrical method in essence calculates all the space inside the unit cell that surrounds the framework atoms.

2.2. MD Simulations

Molecular dynamics (MD) simulations were performed in order to determine the micropore transport diffusivities of each of the SMROG components through the pores of the four MOFs studied. The micropore transport diffusivity, D_t, is related to the flux, J, through Fick's law of diffusion as follows:

$$J = -D_t \nabla q \tag{2}$$

It is therefore necessary to evaluate D_t in order to accurately describe the flux of adsorbate molecules through MOF pores. In this work, we make use of the Onsager formulation in order to determine the transport diffusion coefficients of each of the adsorbates through the pores of each of the four MOFs. This method has been described in detail in other works,[42, 43] and a summary of its application for the simplest case, single component diffusion, is provided in the Supplementary Information.

The EF-NEMD simulations in the NVT ensemble were carried out using the Gromacs package.[44] Each simulation was run for 5.5 ns, where the first 0.5 ns were used for equilibration. A temperature of 298 K was maintained using the Nose-Hoover thermostat[45] and a time step of 1 fs was employed. The equilibrium configurations obtained from GCMC simulations at 298 K and 10 bar were used as starting configurations for each MD simulation. An external force of 0.1 to 1.0 kJ/mol/Å was applied to each adsorbate molecule inside the simulation box such that a linear response was achieved. The MOFs were assumed to be rigid, and the framework atoms were fixed at their crystallographic coordinates. The framework atoms and the adsorbate molecules were represented using the same Lennard-Jones parameters that were used in the GCMC simulations, and the Lorentz-Berthelot mixing rules were employed. Electrostatic interactions were calculated using a particle mesh Ewald (PME) technique[46, 47] with a spacing of 0.12 Å. Each NEMD simulation was repeated five times, and the average displacement correlation function (DCF) values were obtained. The statistical errors for the DCFs were determined using the Student t-test with a 95% confidence interval.

2.3. Breakthrough Simulation Details

The breakthrough simulations are performed with our in-house general adsorption cycle simulator. The column model and the numerical algorithms to solve the model are described in detail elsewhere.[15] This simulator implements the mass, momentum and energy balances for an adsorption column and auxiliary units such as valves and feed lines. For the breakthrough simulations only a model for the adsorption column shown in Figure 2 is required.

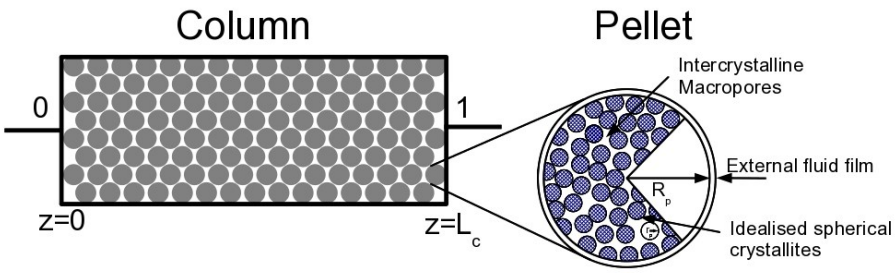

Figure 2. Characteristics of adsorption column model containing adsorbent pellets used in the breakthrough simulations. The inset shows a pellet of radius R_p, containing spherical crystallites separated by intercrystalline macropores.

The model assumes that the mixture behaves as an ideal gas at the reference temperature. A dual-site Langmuir model is used to describe the adsorption process, and the pressure drop is described by the Ergun equation. An axially dispersed plug flow model is employed. The non-isothermal process is modeled by accounting for heat transfer between the column wall and the bed, as well as between the column wall and the surroundings. The temperature inside the adsorbent pellets is assumed to be uniform. Detailed mass and energy balances are provided in the Supporting Information.

The velocity at the column inlet is set and the outflow velocity is calculated from the mass balance. Initially the column is at uniform pressure, temperature and gas phase concentration. The adsorbate concentration is assumed to be in equilibrium with the set gas phase concentration.

The governing partial differential algebraic equations are discretized along the spatial dimension with a flux-limited finite volume method[15] and the resulting set of ordinary differential algebraic equations is integrated in time with the variable time step, variable order backward differentiation formulas implemented in SUNDIALS.[48]

The column characteristics and operating conditions were maintained constant for all materials and were taken from Ribeiro et al, including a feed flow rate of 12.2 m^3/h, and an inlet pressure of 7 bar.[16] SMROG feed is normally available between 21 and 38°C[11], therefore the feed temperature was set to a value within this range, that is 298 K. The mixture composition was defined as shown in Table 1. A complete list of simulation parameters is provided in the Supporting Information.

Table 1. Feed gas composition (SMROG)[16]

	Composition (mole%)
H_2	73.0
CO_2	16.0
CO	3.0
CH_4	4.0
N_2	4.0

Single component and binary mixture adsorption isotherms for each of the four MOFs as well as the isosteric heats of adsorption and Henry constants were calculated using GCMC simulations and fitted to the dual-site Langmuir (DSL) model using the weighted least squares fitting detailed in the work of Brandani and Ruthven.[49] The model parameters were determined by simultaneously fitting single component and binary mixture data while satisfying Henry constant restrictions. As shown in Figure 3 the DSL curves were in good agreement with the simulated isotherms. Furthermore the fitted parameters were able to predict correctly binary mixture selectivities for each of the four frameworks presented in Figure 4. It should be noted that although the DSL model as formulated here does not account for the impact of fugacity on adsorption, the PSA simulations in which they were employed were carried out for inlet

pressures ranging from 5 to 20 bar. Isotherm fitting was focused on the low pressure region corresponding to the partial pressure of each mixture component, where the ideal gas law is a reasonable approximation. The fitted pure component isotherm parameters, provided in the Supplementary Information, were used directly as inputs for the transient breakthrough simulations. In the case of Zeolite 5A and Calgon PCB as well as the commercial zeolite and activated carbon described by Ribeiro et al., isotherm parameters found in the literature[16, 17] were refitted to the dual-site Langmuir model.

Kinetic properties were represented using a bidisperse porous model, where macropore and micropore diffusivities are treated as resistances in series. Single component micropore transport diffusivities for the MOFs were calculated using EF-NEMD simulations and are given in

Table **2**, while the micropore diffusivities for the commercial zeolite and activated carbon were taken from Ribeiro et al.[16] In the case of Zeolite 5A and Calgon PCB, the dominant resistance was assumed to be the diffusion of molecules through the macropores, therefore micropore diffusion was not needed in the predictions obtained from the breakthrough model. The macropore diffusivities were determined using molecular diffusivities alone, which were calculated according to the Chapman-Enskog equation.[50] Macropore diffusivity calculation details are provided in the Supplementary Information.

Table 2. Micropore Transport Diffusivities calculated from EF-EMD simulations

Adsorbate	Micropore Transport Diffusivity $D_c \times 10^9 (m^2/s)$			
	UiO-66(Zr)	UiO-66(Zr)-Br	UiO-67(Zr)	Zr-Cl_2AzoBDC
H_2	44.5 ± 3.23	10.80 ± 1.23	154.00 ± 1.28	193.00 ± 3.33
CO_2	5.96 ± 0.30	2.80 ± 0.30	26.60 ± 1.80	31.70 ± 0.89
CO	5.83 ± 0.59	0.46 ± 0.06	23.40 ± 1.13	34.60 ± 1.94
CH_4	8.25 ± 0.68	0.22 ± 0.04	23.10 ± 2.12	28.10 ± 1.45
N_2	4.46 ± 0.65	0.25 ± 0.05	22.80 ± 1.45	28.70 ± 2.38

The relative impact of these micropore diffusivities was compared to the macropore diffusivities using the criterion developed by Ruthven and Loughlin[51] as shown in equation (3).

$$\gamma = \frac{D_c / r_c^2 (1+K)}{D_p / r_p^2} \tag{3}$$

$$\text{where } K = \frac{(1-\varepsilon_p) H_{ad}}{\varepsilon_p} \quad \text{and} \quad H_{ad} = \frac{\rho_s \mathrm{R} T H}{M_w}$$

Here D_c and D_p are the micropore and macropore diffusivities through crystallites and pellets of radii of r_c and r_p, respectively, and H denotes the Henry constant. The γ parameters evaluated for the four MOFs are given in **Error! Reference source not found.**. For $\gamma < 0.1$ the process is micropore diffusion limited, while for $\gamma > 10$ macropore diffusion is the governing process. In the case of $0.1 < \gamma < 10$ both macropore and micropore diffusion must be taken into account. The crystallite and pellet radii were set to 3 μm and 0.85 mm, respectively. The crystallite size was chosen at the high end of the Zr MOF crystal size range[52], in order to account for the longest possible micropore diffusion path. As all calculated γ values are greater than 10, the macropore diffusion process is much slower than diffusion through the micropores. We can therefore

conclude that for all mixture components and for all four MOFs the uptake rate is macropore diffusion limited.

Table 3. Micropore/macropore comparison criterion, γ

	UiO-66(Zr)	UiO-66(Zr)-Br	UiO-67(Zr)	Zr-Cl_2AzoBDC
H_2	2,037	491	7,379	9,105
CO_2	39,492	54,095	49,277	31,414
CO	4,556	555	8,515	9,241
CH_4	19,010	915	22,992	15,363
N_2	2,376	178	5,991	6,246

3. Results and Discussion

Table 4. Simulated isosteric heats of adsorption at 7 bar and 300 K for each of the mixture components, as well as free volumes and pore sizes for the four MOFs studied.

Material	Δh (kJ/mol)					Void Fraction	Pore Volume (cm^3/g)	Pore Size (Å)
	H_2	CO_2	CO	CH_4	N_2			
UiO-66(Zr)	6.75	26.53	15.89	18.60	14.62	0.586	0.482	6.6, 7.5
UiO-66(Zr)-Br	7.46	29.67	18.22	21.00	16.69	0.526	0.330	6.4, 7.3
UiO-67(Zr)	5.01	20.37	11.89	14.17	10.69	0.716	1.011	8.9, 9.7, 11.9
Zr-Cl_2AzoBDC	4.69	17.28	11.31	13.51	10.37	0.748	1.118	10.4, 11.8, 13.6

3.1. Pure Component Adsorption Isotherms

The adsorption isotherms of each of the impurities in the four structures investigated were determined through GCMC simulations up to a pressure of 50 bar, and are shown in Figure 3.

They provide information not only about the relative capacities of the MOFs, but also about the relative strength of the adsorbate-framework interactions. Many studies have shown that the adsorption properties of MOFs are governed by a combination of the free volume and the enthalpy of adsorption.[53-55] The influence of the free volumes and adsorption enthalpies presented in

Table **4** on the isotherms shown in Figure 3 is a reflection of this relationship. At high pressure, the highest uptake of all four adsorbates occurs in UiO-67(Zr). Although Zr-Cl_2AzoBDC has a higher pore volume than UiO-67(Zr), and chlorine functionalized linkers, the slightly shorter linkers of UiO-67(Zr) lead to narrower pores and at the same time to stronger dispersion interactions. At high pressure, the UiO-66(Zr) and UiO-66(Zr)-Br frameworks show the lowest volumetric uptake for each of the adsorbates due to their lower pore volumes as shown in

Table **4**. At low pressure on the other hand, these smaller pore MOFs have the highest uptake of all four adsorbates. As shown in

Table **4**, the highest enthalpies of adsorption for CO, N_2, CH_4 and CO_2 are observed in UiO-66(Zr)-Br. This can be explained by the presence of narrow pores and pore windows and bromine functional groups, which result in strong dispersion and electrostatic interactions, respectively. It is interesting to note, however, that in the case of CO and N_2 adsorption, all four frameworks have very similar uptake up to a pressure of 20 bar. The highest N_2 enthalpy of adsorption was observed in UiO-66(Zr)-Br, followed by the unfunctionalized UiO-66(Zr), however N_2-framework interactions are relatively weak compared to the other impurities that must be removed during H_2 purification. As a result N_2 will be the most weakly retained impurity, and its breakthrough time dictates the length of the PSA feed step.[3] It is therefore

particularly important to identify materials that can selectively adsorb N_2 from H_2 fuel sources such as SMROG.

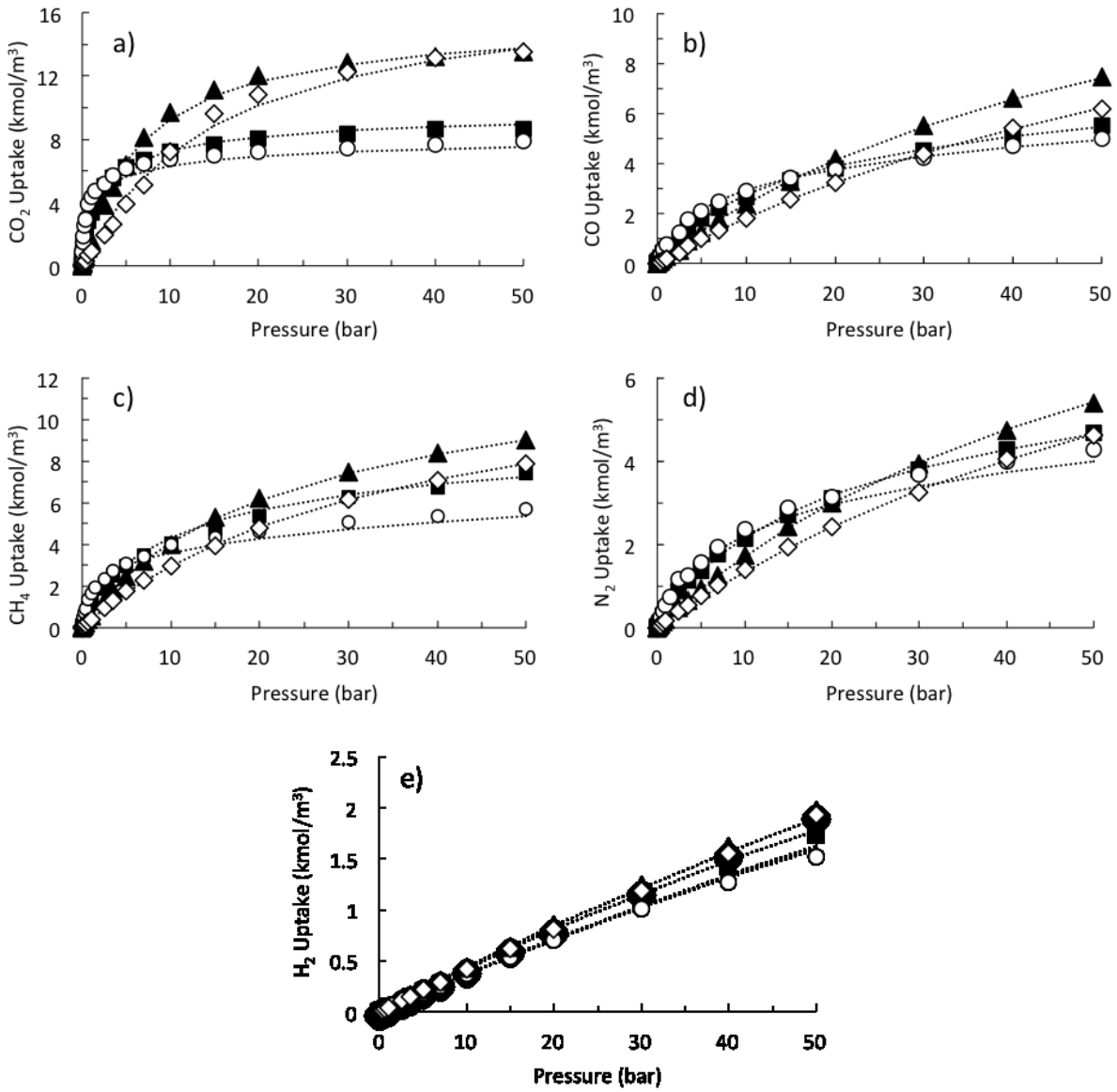

Figure 3. Pure component adsorption isotherms obtained using GCMC simulations for a) CO_2, b) CO, c) CH_4, d) N_2 and e) H_2 in each of the four MOFs investigated. UiO-67(Zr) – filled triangles, Zr-Cl_2AzoBDC – open diamonds, UiO-66(Zr)– filled squares, UiO-66(Zr)-Br – open spheres. The dotted lines represent the dual-site Langmuir fitted curves. Loading is expressed in volumetric terms, where the volume represents the space taken up only by MOF crystallites.

3.2. Adsorption of Binary Mixtures

In order to evaluate the ability of each MOF to selectively adsorb CH_4, CO_2, CO and N_2 from SMROG streams, GCMC simulations were performed for binary mixtures of CH_4:H_2, CO:H_2, CO_2:H_2, and N_2:H_2. The hydrogen content of a SMROG mixture is normally at least 70%, therefore the binary mixture simulations were carried out on mixtures with impurity:H_2 ratios of 30:70. By maintaining the hydrogen content constant across all four mixtures we are able to not only compare the selectivities of the four MOFs for each of the impurities, but also the degree of selectivity relative to the impurity to be removed. It should be noted that in a PSA column the ratio of impurity to H_2 gas is significantly lower, particularly at the leading edge of the concentration front.

The binary mixture adsorption data was used in order to determine the selectivities for each of the impurities, which are shown as a function of pressure in Figure 4. The highest selectivities for all four impurities are observed in UiO-66(Zr)-Br. This behavior is a result of the significant potential overlap caused by a narrow pore size, as well as the presence of Br functional groups, both of which lead to increased interactions between the adsorbate molecules and the framework. The lowest CO_2, CH_4, N_2 and CO selectivities correspond to the large pores of UiO-67(Zr) and Zr-Cl_2AzoBDC, where the adsorption enthalpies are the lowest.

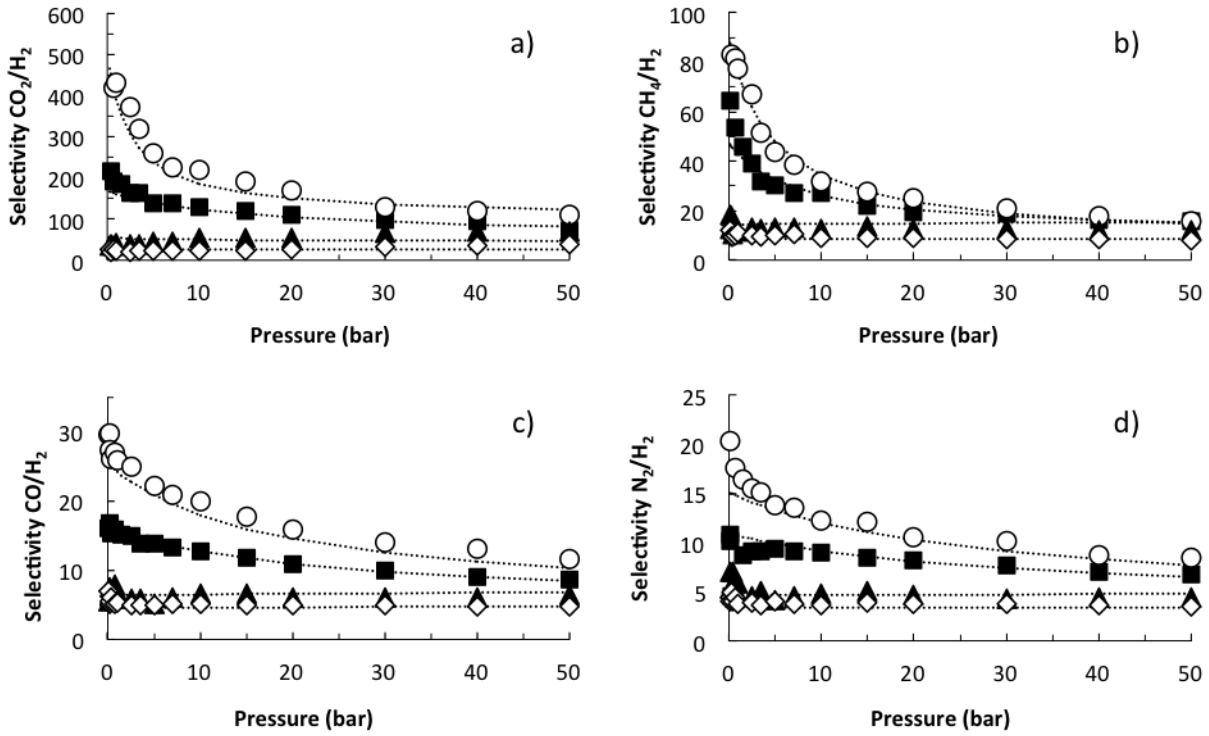

Figure 4. Selectivities from binary mixture adsorption of a) CO_2:H_2 30:70, b) CH_4:H_2 30:70, c) CO:H_2 30:70, and d) N_2:H_2 30:70. UiO-67(Zr) – filled triangles, Zr-Cl_2AzoBDC – open diamonds, UiO-66(Zr) – filled squares, UiO-66(Zr)-Br – open spheres. The dotted lines represent the dual-site Langmuir fitted curves.

The working capacities of each MOF, that is the amount of CH_4, CO_2, CO and N_2 that can be adsorbed from each binary mixture at the PSA feed pressure less what remains adsorbed at the purge pressure, were calculated for a 1-7 bar process:

$$\Delta q_i = q_{i,7bar} - q_{i,1bar} \quad (4)$$

The isothermal working capacity, Δq_i, is a particularly useful measure, as it gives insight into the ease of regeneration of a MOF, as well as its ability to capture impurities. Note, that during a PSA process the temperature inside the bed increases during the adsorption process resulting in a

decrease of the working capacity. However the isothermal working capacities presented here provide a suitable measure for comparing different adsorbents. As shown in **Figure 5**, the highest CO and N_2 working capacities correspond to UiO-66(Zr)-Br where stronger adsorbate-framework interactions result in higher uptake at 7 bar than in the other three MOFs. At 1 bar, uptake of CO and N_2 is low in all four structures. UiO-66(Zr) has the highest CH_4 and CO_2 working capacity due to strong adsorbate-framework interactions, as well as a higher pore volume than UiO-66(Zr)-Br. Interestingly, UiO-67(Zr) has a higher CO_2 working capacity than UiO-66(Zr)-Br, in spite of a large difference in adsorption enthalpies. This indicates that unlike the working capacities of weaker adsorbates, which depend mainly on the enthalpies of adsorption, the amount of CO_2 adsorbed during a PSA cycle is also dependent on the pore volume available. Figure S3 and S4 of the Supporting Information show the working capacities corresponding to the impurity partial pressures in an SMROG stream operating between 1 bar and 7 bar, and from 1 bar and 20 bar, respectively. The highest working capacities for CO, N_2 and CH_4 for both SMROG equivalent pressure ranges were found to correspond to UiO-66(Zr)-Br. The highest CO_2 working capacities correspond to UiO-66(Zr) and UiO-66(Zr)-Br in the low pressure range, and to UiO-66(Zr) and UiO-67(Zr) in the high pressure range. CO_2 is the most abundant impurity present in an SMROG stream, typically 15-25%[3], and interacts strongly with all four MOFs studied. As CO_2 molecules are more competitively adsorbed in a PSA bed than CH_4, CO and N_2 molecules, they displace the more weakly interacting impurities from the adsorption sites, effectively "pushing" them to adsorption sites further up the column.

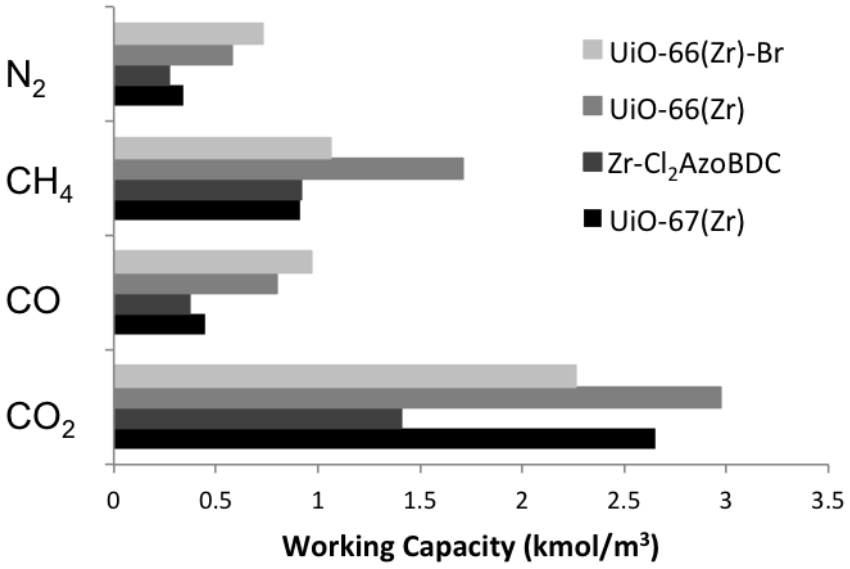

Figure 5. Working capacities from binary mixture simulations, for all impurities for a PSA operating range of 1-7 bar, and 298 K.

The selectivity plots as well as the working capacities present valuable information about the potential of each MOF as a PSA adsorbent for H_2 purification. However, our results show that a MOF might be very promising in some aspects while showing limitations in others. Based on its high selectivities and N_2 and CO working capacities, UiO-66(Zr)-Br appears to have the greatest ability to retain weakly interacting impurities. Its small pore volume, and hence its lower CO_2 and CH_4 working capacities however, may lead to a shorter overall breakthrough time. UiO-66(Zr) on the other hand, which also exhibits relatively high selectivities, has high CO_2 and CH_4 working capacities and is expected to display good retention of these strongly interacting impurities. Its lower N_2 and CO selectivities however, could lead to a quicker elution of these impurities into the outlet stream. It is difficult to use this information alone in order to determine which material would be able to selectively adsorb the largest amount of impurities, allow for the

longest PSA feed step, as well as require the lowest amount of purge gas during the regeneration step.

3.3. Breakthrough Curves

In the work of Ribeiro et al., PSA cycles were modeled using five component SMROG mixtures and layered beds composed of a commercial zeolite and an activated carbon.[16] Here we compare beds containing these commercial adsorbents to beds containing the four MOFs, UiO-66(Zr), UiO-66(Zr)-Br, UiO-67(Zr) and Zr-Cl_2AzoBDC as well as Zeolite 5A and Calgon PCB.

The breakthrough curves in Figure 6 show the concentration of each impurity as a function of dimensionless time at the column outlet. The dimensionless time, τ, was calculated using

$$\tau = {tu}/{\varepsilon L} \qquad (5)$$

Where u is the velocity of the mixture through the column, L is the column length, and ε is the bed void fraction. The use of dimensionless breakthrough time as opposed to specific time allows for a direct comparison of the breakthrough behavior between processes with different operating parameters. As shown in Figure 6, for all six adsorbents, the first impurity to elute is N_2, followed by CO, CH_4 and finally CO_2 as expected considering the weak N_2-pore surface interactions, and the high heats of adsorption of CO_2 in each of the materials. N_2 breakthrough is therefore confirmed as the limiting factor in determining the duration of the feed step in the PSA process. In addition, the strong interactions between CO_2 and the adsorbents indicate that this impurity is the most difficult to desorb, and could therefore present a constraint during the purge step. In the four MOFs and the activated carbon, CO is adsorbed more weakly than CH_4, and therefore elutes more quickly. Conversely in the commercial zeolite, the nonpolar CH_4 molecules

interact more weakly with the framework, and therefore elute earlier than the polar CO molecules. The breakthrough curves of the three intermediate compounds adsorbed, that is N_2, CH_4, and CO, contain regions where the outlet concentrations are higher than their concentrations in the inlet stream. These regions contain one, two or three plateaus each, depending on the order of elution, and are caused by a competitive adsorption behavior, where more strongly adsorbed species displace weaker interacting species from adsorption sites within the column. For example, in Figure 6 a) the N_2 curve presents three consecutive steps signifying the displacement of N_2 molecules by CO, CH_4 and CO_2 molecules, respectively.

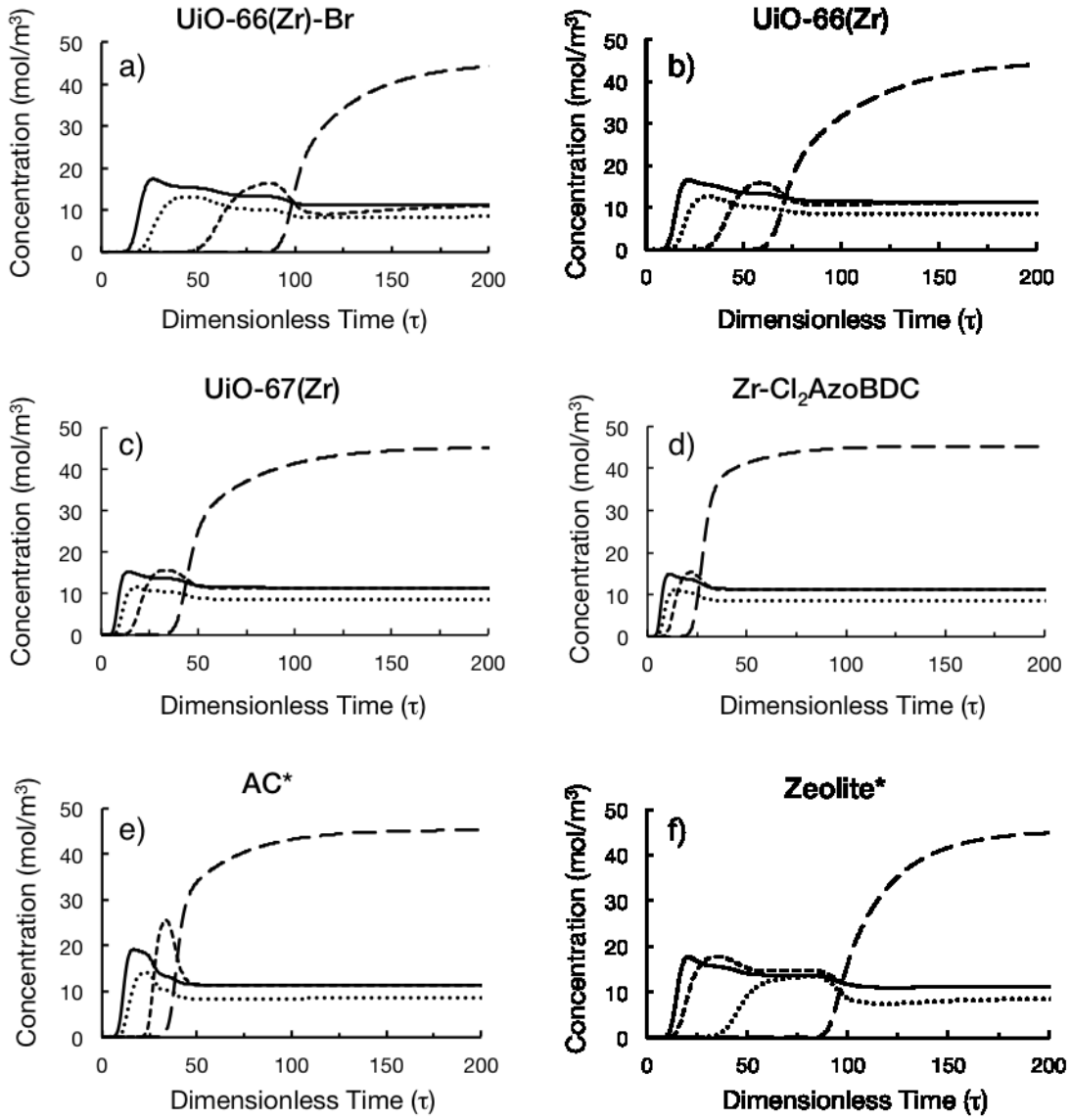

Figure 6. Simulated breakthrough curves for a five component mixture through a 1 m long adsorption column containing a) UiO-66(Zr)-Br b) UiO-66(Zr) c) UiO-67(Zr) d) Zr-Cl_2AzoBDC e) AC* f) Zeolite*. long dashed line – CO_2, short dashed line – CH_4, dotted line – CO, solid line – N_2. Zeolite* and AC* are the commercial adsorbents from the work of Ribeiro et al. [16]

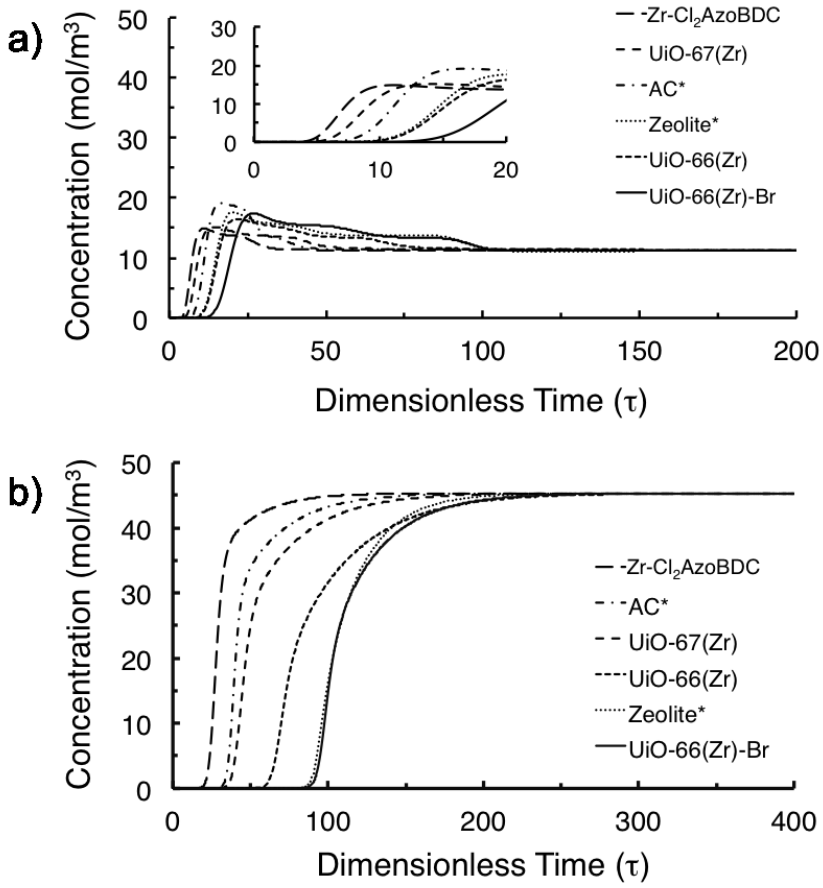

Figure 7. a) N_2 and b) CO_2 outlet concentrations as a function of dimensionless time for each of the six adsorbents. The inset in a) focuses on the 0-20 range. Zeolite* and AC* are the commercial adsorbents from the work of Ribeiro et al. [16]

We focus on the N_2 and CO_2 breakthrough curves shown in Figure 7 in order to determine how MOFs perform in comparison with the commercial zeolite and activated carbon. Two of the four MOFs considered, namely UiO-66(Zr) and UiO-66(Zr)-Br, have longer N_2 breakthrough times than the zeolite, suggesting that these materials could potentially be used to replace zeolites in hydrogen purification beds in order to optimize the PSA process. The inset in Figure 7 a) shows UiO-66(Zr)-Br to have the longest time to breakthrough for N_2 molecules, which makes it the most promising MOF in this study. UiO-67(Zr) and Zr-Cl_2AzoBDC both have significantly

shorter N_2 breakthrough times than the zeolite. Figure 7 b) shows that the CO_2 breakthrough time of UiO-66(Zr)-Br is similar to that of the zeolite. CO_2 adsorbs weakly in the activated carbon, as well as the large pore MOFs and therefore elutes at an earlier time point.

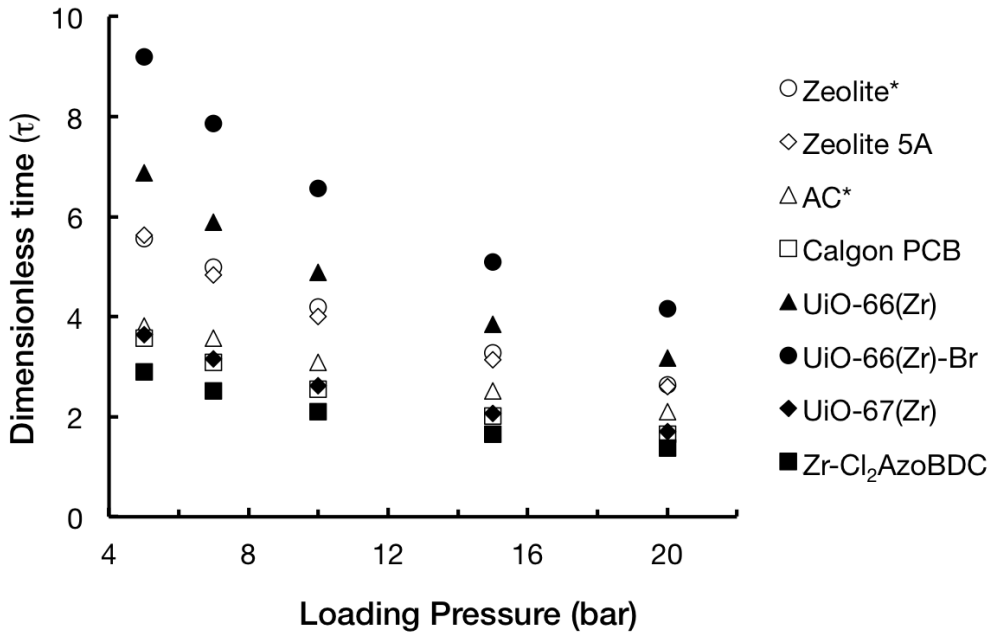

Figure 8. N_2 breakthrough time as a function of loading pressure. Zeolite* and AC* are the commercial adsorbents from the work of Ribeiro et al. [16]

In order to compare the performance of the four MOFs to industrial PSA adsorbents, we extended our analysis to include Zeolite 5A and activated carbon Calgon PCB, which have been widely studied. Breakthrough simulations for these materials were carried out based on the adsorption data provided in the recent PSA work of Ahn et al.[40] In Figure 8 breakthrough times for the MOFs, zeolites and activated carbons are plotted as a function of loading pressure. For all adsorbents in this study N_2 is the first impurity to elute into the product stream. Considering that the purity requirement for H_2 fuel and propellant applications is a N_2 concentration lower than 2

ppm[56], the breakthrough time was defined as the time at which the N_2 content in the outlet stream reaches a conservative 1 ppm.

UiO-67(Zr) and Zr-Cl_2AzoBDC have short breakthrough times across the entire pressure range, similar to the activated carbons, which is due to weak N_2 framework interactions. The remaining two MOFs however, have longer breakthrough times than the two zeolite materials. The longest retention of impurities corresponds to UiO-66(Zr)-Br, making this a particularly promising PSA adsorbent.

As mentioned earlier, the length of the PSA purge step is limited by the ease of CO_2 desorption from the bed. Currently, PSA units employ layered beds containing two or more adsorbents. This technique aims to adsorb each impurity within a layer from which it can be readily desorbed. Alumina or silica layers are used to adsorb water vapor, while activated carbon is used to target CO_2 and long hydrocarbons. These strongly adsorbing impurities are thus prevented from reaching the zeolite layer, from which they would be difficult to remove. In the work of Ribeiro et al., a layered bed containing activated carbon and zeolite is modeled as part of an eight-step PSA cycle, and an outlet stream purity of 99.9994% is obtained.[16] Considering that some MOFs in this study have high heats of adsorption for CO_2, particularly UiO-66(Zr)-Br, it is likely that the use of MOFs in layered adsorption beds along with activated carbon will prove to be more efficient than the use of a MOF-only bed.

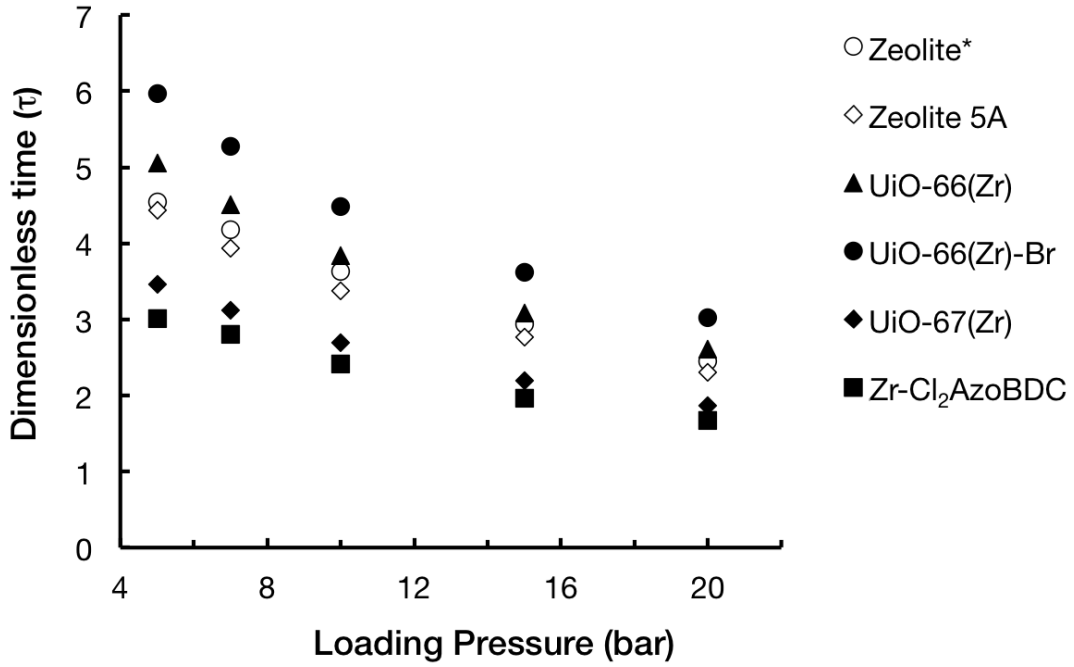

Figure 9. N_2 breakthrough time for layered beds as a function of loading pressure. Each bed contains an AC* layer and an equal layer of MOF or zeolite. Zeolite* and AC* are the commercial adsorbents from the work of Ribeiro et al.[16]

Breakthrough curves were modeled for the same gas mixture through 1 m long columns containing a 0.5 m bottom layer of the commercial activated carbon used by Ribeiro et al., followed by a 0.5 m layer of each of the MOFs and the commercial zeolite. The UiO-66(Zr) and UiO-66(Zr)-Br layered bed show similar or longer N_2 breakthrough times than the two zeolite layered beds as shown in Figure 9. Generally N_2 breakthrough times are shorter in the case of layered beds than for the single component beds due to the relatively fast movement of molecules through the AC layer. A comparison of the N_2 time to breakthrough for single versus two-layered beds is shown in Figure 10. While the addition of an AC layer has the benefit of capturing CO_2 molecules and preventing them from reaching the MOF layer, there is a trade-off

in terms of feed step duration, and this effect is most significant in the case of UiO-66(Zr)-Br. Nevertheless, while both UiO-66(Zr) and UiO-66(Zr)-Br perform better than the commercial zeolite of Ribeiro et al. and Zeolite 5A, the most promising framework for H_2 purification using a two-layered bed is UiO-66(Zr)-Br. In UiO-67(Zr) there is only a minor decrease in breakthrough time when the AC layer is included, while in the Zr-Cl_2AzoBDC breakthrough time is actually improved in the two layer setup. This is explained by a weak retention of CO_2 in the two large pore MOFs as shown in Figure 7 b), which is similar or worse than that of AC*.

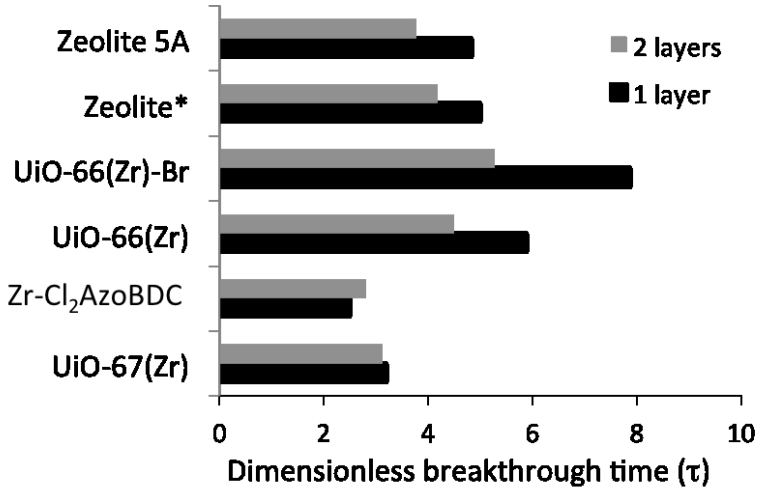

Figure 10. Time to N_2 breakthrough (1 ppm in the outlet stream) for 1 m columns containing MOF or zeolite only (black), and layered columns containing equal volumes of AC* and MOF or zeolite (grey). Zeolite* and AC* are the commercial adsorbents from the work of Ribeiro et al.[16]

In order to compare the ease of column regeneration, layered bed adsorption simulations were carried out for each of the MOFs and zeolites and terminated at their specific N_2 breakthrough times. These simulations were then succeeded by a desorption stage carried out at 1 bar, consisting of a 50 s blow-down and a 450 s purge with pure H_2. The impurity loadings at the bottom of the MOF/zeolite layer, approximately in the middle of the column, during the

adsorption and desorption stages are shown on the left and right hand sides of **Figure 11**, respectively. Unsurprisingly the lowest loading during adsorption, and quickest regeneration is observed in UiO-67(Zr) and Zr-Cl_2AzoBDC. The two smaller pore MOFs, UiO-66(Zr) and UiO-66(Zr)-Br have the highest impurity loading following the adsorption stage. In particular, UiO-66(Zr)-Br has a N_2 loading that is more than three times those in Zeolite* and Zeolite 5A. Despite the higher amounts of impurities adsorbed inside the small-pore MOFs, full regeneration is achieved after approximately 300 s, which is nearly the same as the regeneration times observed for the two zeolites. This indicates that a layered PSA column containing UiO-66(Zr) or UiO-66(Zr)-Br could be used in order to produce a greater amount of high purity H_2 than the two zeolites, without requiring a longer purge stage.

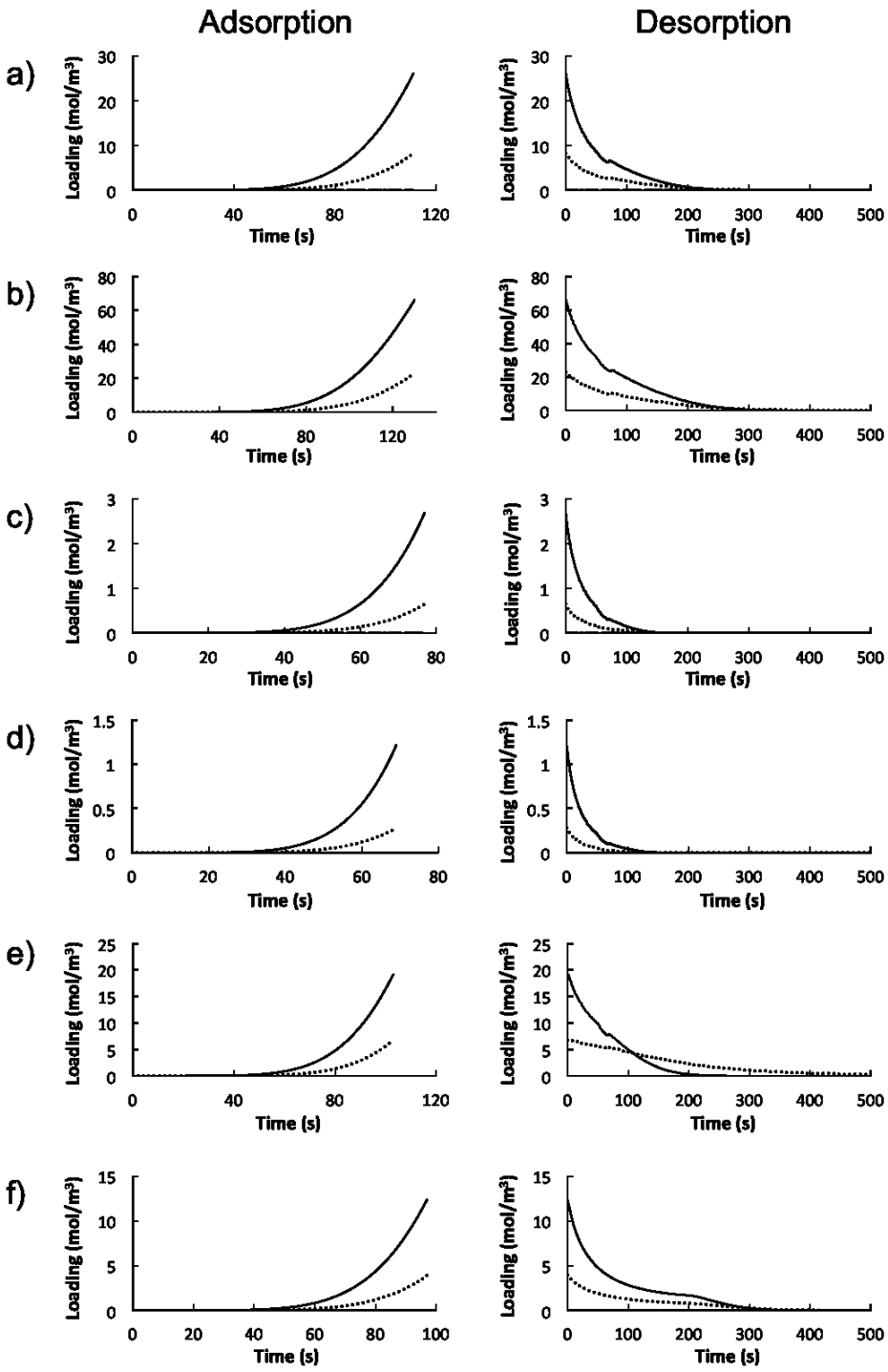

Figure 11. Adsorbed impurity concentrations at the bottom of the MOF/zeolite layer from layered bed adsorption simulations terminated at the N_2 breakthrough point (left column) and desorption simulations (right column). Beds contain equal layers of AC* and a) UiO-66(Zr) b)

UiO-66(Zr)-Br c) UiO-67(Zr) d) Zr-Cl_2AzoBDC e) Zeolite* and f) Zeolite 5A. Dotted line – CO, solid line – N_2, long dashed line – CO_2, short dashed line – CH_4. The CO_2 and CH_4 curves coincide with the x-axes in all cases. Zeolite* and AC* are the commercial adsorbents from the work of Ribeiro et al.[16]

For all of the frameworks investigated here, the chosen activated carbon layer height of 0.5 m was observed to prevent CO_2 from eluting into the MOF layer before the N_2 breakthrough time was reached. Given the substantial reduction in the overall N_2 breakthrough time caused by the AC layer addition, only the minimum amount of AC required to retain the CO_2 molecules should be used. We selected the structure identified as having the longest N_2 breakthrough time, UiO-66(Zr)-Br in order to investigate the optimum AC layer height. In Figure 12 a plot of the CO_2 AC layer breakthrough time is shown along with the overall N_2 breakthrough time for a range of AC and UiO-66(Zr)-Br layer height ratios. The column length was maintained fixed at 1 m. For an AC layer height between 0.2 and 0.4 m, CO_2 (shown as empty spheres) reaches the UiO-66(Zr)-Br layer before the N_2 concentration (shown as filled spheres) reaches 1 ppm in the product stream. In this region, the duration of the PSA cycle is limited by the CO_2 breakthrough time through the activated carbon. For an AC layer thicker than 0.45 m, all of the CO_2 is retained inside the AC layer for much longer periods of time. However, a thicker activated carbon layer results in poorer N_2 retention. In the case of an AC layer height larger than 0.45 m the PSA cycle duration is limited by the N_2 breakthrough time, which is significantly shorter. The operating range is therefore the area underneath the lowest of the two constraints, and is shown in grey in Figure 12 .The shortest AC layer height that would render a CO_2 retention time in the AC layer that is longer than the N_2 overall retention time is 0.45 m. Decreasing the AC layer length from

0.5 m to 0.45 m would increase the potential PSA dimensionless breakthrough time from 5.27 to 5.47 (130 s to 135 s).

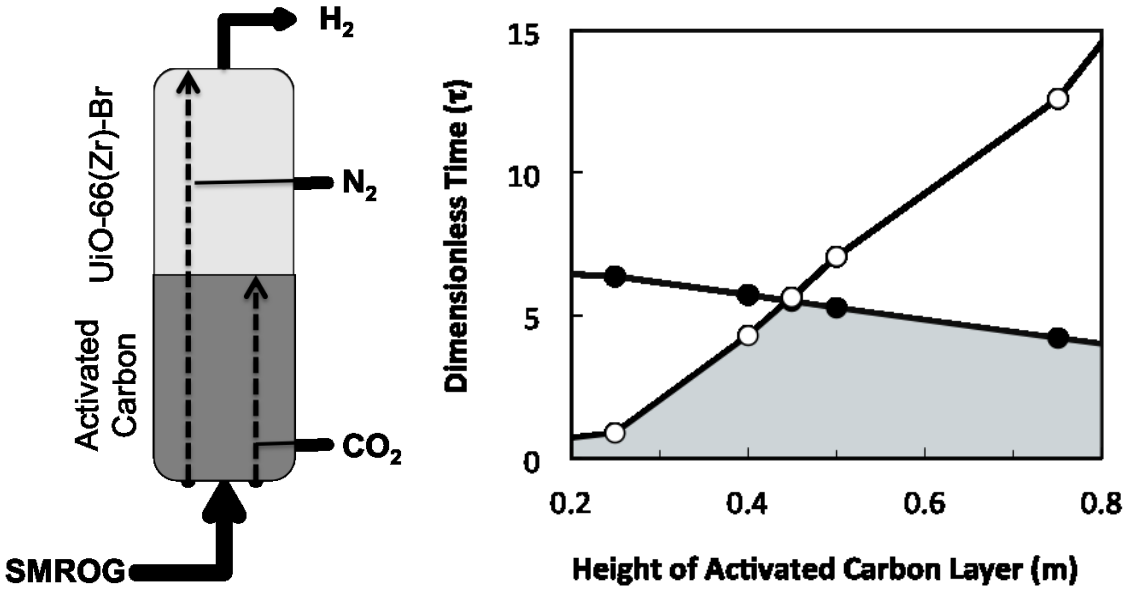

Figure 12. For a layered bed of the commercial activated carbon and UiO-66(Zr)-Br: 1 ppm breakthrough time for CO_2 at the end of the activated layer (open spheres) and the N_2 breakthrough time at the end of the column (filled spheres). The grey shaded region in the graph denotes the PSA cycle durations for which both operating conditions are satisfied: N_2 retention inside the column and CO_2 retention in the activated carbon layer.

4. Conclusions

The work presented in this study demonstrates that some metal-organic frameworks may be able to compete with commercial zeolites as adsorbents for the purification of H_2 from SMROG via pressure swing adsorption. The separation capabilities of four MOFs, namely UiO-66(Zr), UiO-66(Zr)-Br, UiO-67(Zr) and Zr-Cl_2AzoBDC were compared to a commercial zeolite and a commercial activated carbon, as well as Zeolite 5A and Calgon PCB. The MOFs were first

evaluated in terms of their pure component adsorption isotherms, working capacities, and adsorption enthalpies for each of the mixture components, as well as binary mixture selectivities. UiO-66(Zr)-Br was observed to have the highest selectivities and working capacities for N_2 and CO, indicating that the presence of narrow pores and functionalized linkers results in improved retention of weakly interacting gases due to stronger adsorbate – framework interactions. UiO-66(Zr) on the other hand displayed the highest CH_4, and CO_2 working capacities for a 1-7 bar pressure range. Considering that CO_2 is the most abundant impurity in the SMROG mixture, and that the most weakly adsorbed impurity is N_2, it is difficult to determine which of the four MOFs would be most efficient in separating H_2 from SMROG based on adsorption and selectivity data alone. We therefore employed breakthrough curve simulations for five component mixtures composed of H_2, N_2, CO, CH_4 and CO_2. These simulations are exceptionally useful as it enables the study of both, adsorptive and diffusive processes, and takes into account the contributions of each of the mixture components. The study of single and two-layered beds revealed that UiO-66(Zr) and UiO-66(Zr)-Br have longer breakthrough times than the commercial zeolite studied by Ribeiro et al. and zeolite 5A, and would therefore result in a larger amount of high purity H_2 product per PSA cycle. UiO-66(Zr)-Br was found to be the most effective material for retaining the impurities present in SMROG, having the longest breakthrough time in this study.

It is important to bear in mind that PSA adsorbents are selected not only based on their thermodynamic properties but also on their physical robustness. The UiO-66(Zr) family of MOFs has been shown to have a high resistance to solvents and to mechanical pressure of up to 10 kg/cm^2,[23] making UiO-66(Zr)-Br a particularly promising PSA adsorbent.

Acknowledgements

T.D. and A.-M. B. thank the EPSRC (EP/F009208/1) for funding. D.F and S.B thank the EPSRC (EP/G062129/1 and EP/I010939/1) for funding. This work has made use of the resources provided by the Edinburgh Compute and Data Facility (ECDF) (http://www.ecdf.ed.ac.uk/).

Supporting Information Available

Calculation of micropore and macropore diffusion parameters and Table S1 containing linear driving force parameters for micropore and macropore diffusion. EF-NEMD simulation details. Breakthrough model and simulation details. Table S2 containing the process parameters adopted in the PSA column simulations. Table S3, Table S4 and Table S5 containing dual site Langmuir parameters for the four MOFs, and the zeolites and activated carbons. Validation of breakthrough simulations and Figure S1 showing a comparison of simulated and experimental breakthrough curves. A validation of adsorption isotherm simulations for UiO-66(Zr) is presented in Figure S2. Figures S3 and S4 presenting the MOF working capacities for pressure ranges equivalent to the impurity partial pressures in SMROG, which are included in Table S6. Figures S5 – S8 containing the isosteric heats of adsorption for each of the MOFs as a function of loading. Table S7 containing the estimated bulk densities of the four MOFs studied. This information is available free of charge via the Internet at http://pubs.acs.org/.

References

(1) Ruthven, D. M.; Farooq, S.; Knabel, K. S. *Pressure Swing Adsorption*. VCH: New York, 1994.
(2) Stocker, J.; Whysall, M.; Miller, G. Q. 30 Years of PSA Technology for Hydrogen Purification; 2730; UOP: 1998.
(3) Liu, K.; Song, C.; Subramani, V. *Hydrogen and Syngas Production and Purification Technologies*. American Institute of Chemical Engineers; John Wiley and Sons, Inc. : Hoboken, New Jersey, 2010.
(4) Ritter, J. A.; Yang, R. T. Equilibrium Adsorption of Multicomponent Gas-Mixtures at Elevated Pressures. *Ind. Eng. Chem. Res.* **1987,** *26*, 1679.
(5) Golden, T. C.; Kumar, R.; Kratz, W. C. Hydrogen purification. United States Patent 4957514, 1990.
(6) Plee, D. Purification of hydrogen flowstreams by selectively adsorbing impurities therefrom. United States Patent 6464756, 2002.
(7) Le Bec, R. Method for purifying hydrogen-based gas mixtures using calcium X-zeolite. United States Patent 6849106, 2005.
(8) Bomard, O.; Jutard, J.; Moreau, S.; Vigor, X. Method for purifying hydrogen based gas mixtures using a lithium-exchanged X zeolite. United States Patent 5912422, 1997.
(9) Lee, C. H.; Yang, J. Y.; Ahn, H. W. Effects of carbon-to-zeolite ratio on layered bed H^2 PSA for coke oven gas. *Aiche J.* **1999,** *45*, 535.
(10) Li, J. R.; Sculley, J.; Zhou, H. C. Metal-Organic Frameworks for Separations. *Chem. Rev.* **2012,** *112*, 869.
(11) Sircar, S.; Golden, T. C. Purification of hydrogen by pressure swing adsorption. *Sep. Sci. Technol.* **2000,** *35*, 667.
(12) Krishna, R.; Long, J. R. Screening Metal-Organic Frameworks by Analysis of Transient Breakthrough of Gas Mixtures in a Fixed Bed Adsorber. *J. Phys. Chem. C* **2011,** *115*, 12941.
(13) Ho, M. T.; Allinson, G. W.; Wiley, D. E. Reducing the cost of CO_2 capture from flue gases using pressure swing adsorption. *Ind. Eng. Chem. Res.* **2008,** *47*, 4883.
(14) Kumar, R. Pressure Swing Adsorption Process - Performance Optimum and Adsorbent Selection. *Ind. Eng. Chem. Res.* **1994,** *33*, 1600.
(15) Friedrich, D.; Ferrari, M.-C.; Brandani, S. Efficient Simulation and Acceleration of Convergence for a Dual Piston Pressure Swing Adsorption System, DOI: 10.1021/ie3036349. *Ind. Eng. Chem. Res.* **2013**.
(16) Ribeiro, A. M.; Grande, C. A.; Lopes, F. V. S.; Loureiro, J. M.; Rodrigues, A. E. A parametric study of layered bed PSA for hydrogen purification. *Chem. Eng. Sci.* **2008,** *63*, 5258.
(17) Ahn, S.; You, Y.-W.; Lee, D.-G.; Kim, K.-H.; Oh, M.; Lee, C.-H. Layered two- and four-bed PSA processes for H_2 recovery from coal gas. *Chem. Eng. Sci.* **2012,** *68*, 413.
(18) Lopes, F. V. S.; Grande, C. A.; Rodrigues, A. E. Activated carbon for hydrogen purification by pressure swing adsorption: Multicomponent breakthrough curves and PSA performance. *Chem. Eng. Sci.* **2011,** *66*, 303.
(19) Ahn, H.; Lee, C. H.; Seo, B.; Yang, J.; Baek, K. Backfill cycle of a layered bed H_2 PSA process. *Adsorption* **1999,** *5*, 419.

(20) Ahn, H.; Yang, J.; Lee, C. H. Effects of feed composition of coke oven gas on a layered bed H^2 PSA process. *Adsorption* **2001,** *7*, 339.
(21) Herm, Z. R.; Krishna, R.; Long, J. R. CO_2/CH_4, CH_4/H_2 and $CO_2/CH_4/H_2$ separations at high pressures using Mg_2(dobdc). *Microporous Mesoporous Mater.* **2012,** *151*, 481.
(22) Wu, H. H.; Yao, K. X.; Zhu, Y. H.; Li, B. Y.; Shi, Z.; Krishna, R.; Li, J. Cu-TDPAT, an rht-Type Dual-Functional Metal-Organic Framework Offering Significant Potential for Use in H_2 and Natural Gas Purification Processes Operating at High Pressures. *J. Phys. Chem. C* **2012,** *116*, 16609.
(23) Cavka, J. H.; Jakobsen, S.; Olsbye, U.; Guillou, N.; Lamberti, C.; Bordiga, S.; Lillerud, K. P. A New Zirconium Inorganic Building Brick Forming Metal Organic Frameworks with Exceptional Stability. *J. Am. Chem. Soc.* **2008,** *130*, 13850.
(24) Wu, H.; Yildirim, T.; Zhou, W. Exceptional Mechanical Stability of Highly Porous Zirconium Metal–Organic Framework UiO-66 and Its Important Implications. *J. Phys. Chem. Lett.* **2013,** *4*, 925.
(25) Yang, Q. Y.; Guillerm, V.; Ragon, F.; Wiersum, A. D.; Llewellyn, P. L.; Zhong, C. L.; Devic, T.; Serre, C.; Maurin, G. CH4 storage and CO2 capture in highly porous zirconium oxide based metal-organic frameworks. *Chem. Commun.* **2012,** *48*, 9831.
(26) Biswas, S.; Van der Voort, P. A General Strategy for the Synthesis of Functionalised UiO-66 Frameworks: Characterisation, Stability and CO2 Adsorption Properties. *Eur. J. Inorg. Chem.* **2013**, 2154.
(27) Lopes, F. V. S.; Grande, C. A.; Ribeiro, A. M.; Loureiro, J. M.; Evaggelos, O.; Nikolakis, V.; Rodrigues, A. E. Adsorption of H_2, CO_2, CH_4, CO, N_2 and H_2O in Activated Carbon and Zeolite for Hydrogen Production. *Sep. Sci. Technol.* **2009,** *44*, 1045.
(28) Jee, J. G.; Kim, M. B.; Lee, C. H. Adsorption characteristics of hydrogen mixtures in a layered bed: Binary, ternary, and five-component mixtures. *Ind. Eng. Chem. Res.* **2001,** *40*, 868.
(29) Gupta, A.; Chempath, S.; Sanborn, M. J.; Clark, L. A.; Snurr, R. Q. Object-oriented programming paradigms for molecular modeling. *Mol. Simul.* **2003,** *29*, 29.
(30) Yang, Q.; Wiersum, A. D.; Llewellyn, P. L.; Guillerm, V.; Serre, C.; Maurin, G. Functionalizing porous zirconium terephthalate UiO-66(Zr) for natural gas upgrading: a computational exploration. *Chem. Commun.* **2011,** *47*, 9603.
(31) Haile, J. M. *Molecular Dynamics Simulation: Elementary Methods*. John Wiley & Sons: New York, 1992; p 489.
(32) Ewald, P. P. Die Berechnung optischer und elektrostatischer Gitterpotentiale. *Ann. Phys.* **1921,** *369*, 253.
(33) Rappe, A. K.; Casewit, C. J.; Colwell, K. S.; Goddard, W. A.; Skiff, W. M. UFF, a Full Periodic-Table Force-Field for Molecular Mechanics and Molecular-Dynamics Simulations. *J. Am. Chem. Soc.* **1992,** *114*, 10024.
(34) Yang, Q.; Wiersum, A. D.; Jobic, H.; Guillerm, V.; Serre, C.; Llewellyn, P. L.; Maurin, G. Understanding the Thermodynamic and Kinetic Behavior of the CO_2/CH_4 Gas Mixture within the Porous Zirconium Terephthalate UiO-66(Zr): A Joint Experimental and Modeling Approach. *J. Phys. Chem. C* **2011,** *115*, 13768.
(35) Martin, M. G.; Siepmann, J. I. Transferable potentials for phase equilibria. 1. United-atom description of n-alkanes. *J. Phys. Chem. B* **1998,** *102*, 2569.
(36) Potoff, J. J.; Siepmann, J. I. Vapor-liquid equilibria of mixtures containing alkanes, carbon dioxide, and nitrogen. *Aiche J.* **2001,** *47*, 1676.

(37) Martín-Calvo, A.; Lahoz-Martín, F. D.; Calero, S. Understanding Carbon Monoxide Capture Using Metal–Organic Frameworks. *J. Phys. Chem. C* **2012,** *116*, 6655.
(38) Yang, Q. Y.; Zhong, C. L. Molecular simulation of adsorption and diffusion of hydrogen in metal-organic frameworks. *J. Phys. Chem. B* **2005,** *109*, 11862.
(39) Peng, D.-Y.; Robinson, D. B. A New Two-Constant Equation of State. *Ind. Eng. Chem. Fundam.* **1976,** *15*, 59.
(40) Vuong, T.; Monson, P. A. Monte Carlo Simulation Studies of Heats of Adsorption in Heterogeneous Solids. *Langmuir* **1996,** *12*, 5425.
(41) Gelb, L. D.; Gubbins, K. E. Pore size distributions in porous glasses: A computer simulation study. *Langmuir* **1999,** *15*, 305.
(42) Chempath, S.; Krishna, R.; Snurr, R. Q. Nonequilibrium Molecular Dynamics Simulations of Diffusion of Binary Mixtures Containing Short n-Alkanes in Faujasite. *J. Phys Chem. B* **2004,** *108*, 13481.
(43) Williams, J. J.; Seaton, N. A.; Düren, T. Influence of Surface Groups on the Diffusion of Gases in MCM-41: A Molecular Dynamics Study. *J. Phys. Chem. C* **2011,** *115*, 10651.
(44) Hess, B.; Kutzner, C.; van der Spoel, D.; Lindahl, E. GROMACS 4: Algorithms for Highly Efficient, Load-Balanced, and Scalable Molecular Simulation. *J. Chem. Theory Comput.* **2008,** *4*, 435.
(45) Frenkel, D.; Smit, B. *Understanding Molecular Simulation: From Algorithms to Applications*. Academic Press: San Diego, 1996.
(46) Darden, T.; York, D.; Pedersen, L. Particle Mesh Ewald - An Nlog(N) Method for Ewald Sums in Large Systems. *J. Chem. Phys.* **1993,** *98*, 10089.
(47) Essmann, U.; Perera, L.; Berkowitz, M. L.; Darden, T.; Lee, H.; Pedersen, L. G. A smooth particle mesh Ewald method. *J. Chem. Phys.* **1995,** *103*, 8577.
(48) Hindmarsh, A. C.; Brown, P. N.; Grant, K. E.; Lee, S. L.; Serban, R.; Shumaker, D. E.; Woodward, C. S. SUNDIALS: Suite of nonlinear and differential/algebraic equation solvers. *ACM Trans. Math. Softw.* **2005,** *31*, 363.
(49) Brandani, F.; Ruthven, D. Measurement of Adsorption Equilibria by the Zero Length Column (ZLC) Technique Part 2: Binary Systems. *Ind. Eng. Chem. Res.* **2003,** *42*, 1462.
(50) Bird, R. B.; Stewart, W. E.; Lightfoot, E. N. *Transport Phenomena*. second ed.; Wiley International: Singapore, 2002.
(51) Ruthven, D. M.; Loughlin, K. F. Diffusional Resistance of Molecular-Sieve Pellets. *Can. J. Chem. Eng.* **1972,** *50*, 550.
(52) Schaate, A.; Roy, P.; Godt, A.; Lippke, J.; Waltz, F.; Wiebcke, M.; Behrens, P. Modulated Synthesis of Zr-Based Metal–Organic Frameworks: From Nano to Single Crystals. *Chem. Eur. J.* **2011,** *17*, 6643.
(53) Frost, H.; Düren, T.; Snurr, R. Q. Effects of surface area, free volume, and heat of adsorption on hydrogen uptake in metal-organic frameworks. *J. Phys. Chem. B* **2006,** *110*, 9565.
(54) Frost, H.; Snurr, R. Q. Design requirements for metal-organic frameworks as hydrogen storage materials. *J. Phys. Chem. C* **2007,** *111*, 18794.
(55) Düren, T.; Sarkisov, L.; Yaghi, O. M.; Snurr, R. Q. Design of New Materials for Methane Storage. *Langmuir* **2004,** *20*, 2683.
(56) *CGA G-5.3 Commodity Specification for Hydrogen*. The Compressed Gas Association Inc.: 2004; p 11.

Figure Captions

Figure 1. a) Octahedral and tetrahedral pores of UiO-66(Zr) b) Linkers joining the zirconium clusters in each of the four MOFs

Figure 2. Characteristics of adsorption column model containing adsorbent pellets used in the breakthrough simulations. The inset shows a pellet of radius R_p, containing spherical crystallites separated by intercrystalline macropores.

Figure 3. Pure component adsorption isotherms obtained using GCMC simulations for a) CO_2, b) CO, c) CH_4, d) N_2 and e) H_2 in each of the four MOFs investigated. UiO-67(Zr) – filled triangles, Zr-Cl_2AzoBDC – open diamonds, UiO-66(Zr)– filled squares, UiO-66(Zr)-Br – open spheres. The dotted lines represent the dual-site Langmuir fitted curves. Loading is expressed in volumetric terms, where the volume represents the space taken up only by MOF crystallites.

Figure 4. Selectivities from binary mixture adsorption of a) CO_2:H_2 30:70, b) CH_4:H_2 30:70, c) CO:H_2 30:70, and d) N_2:H_2 30:70. UiO-67(Zr) – filled triangles, Zr-Cl_2AzoBDC – open diamonds, UiO-66(Zr) – filled squares, UiO-66(Zr)-Br – open spheres. The dotted lines represent the dual-site Langmuir fitted curves.

Figure 5. Working capacities from binary mixture simulations, for all impurities for a PSA operating range of 1-7 bar, and 298 K.

Figure 6. Simulated breakthrough curves for a five component mixture through a 1 m long adsorption column containing a) UiO-66(Zr)-Br b) UiO-66(Zr) c) UiO-67(Zr) d) Zr-Cl_2AzoBDC e) AC* f) Zeolite*. long dashed line – CO_2, short dashed line – CH_4, dotted

line – CO, solid line – N_2. Zeolite* and AC* are the commercial adsorbents from the work of Ribeiro et al. [16]

Figure 7. a) N_2 and b) CO_2 outlet concentrations as a function of dimensionless time for each of the six adsorbents. The inset in a) focuses on the 0-20 range. Zeolite* and AC* are the commercial adsorbents from the work of Ribeiro et al. [16]

Figure 8. N_2 breakthrough time as a function of loading pressure. Zeolite* and AC* are the commercial adsorbents from the work of Ribeiro et al. [16]

Figure 9. N_2 breakthrough time for layered beds as a function of loading pressure. Each bed contains an AC* layer and an equal layer of MOF or zeolite. Zeolite* and AC* are the commercial adsorbents from the work of Ribeiro et al.[16]

Figure 10. Time to N_2 breakthrough (1 ppm in the outlet stream) for 1 m columns containing MOF or zeolite only (black), and layered columns containing equal volumes of AC* and MOF or zeolite (grey). Zeolite* and AC* are the commercial adsorbents from the work of Ribeiro et al.[16]

Figure 11. Adsorbed impurity concentrations at the bottom of the MOF/zeolite layer from layered bed adsorption simulations terminated at the N_2 breakthrough point (left column) and desorption simulations (right column). Beds contain equal layers of AC* and a) UiO-66(Zr) b) UiO-66(Zr)-Br c) UiO-67(Zr) d) Zr-Cl_2AzoBDC e) Zeolite* and f) Zeolite 5A. Dotted line – CO, solid line – N_2, long dashed line – CO_2, short dashed line – CH_4. The CO_2 and CH_4 curves coincide with the x-axes in all cases. Zeolite* and AC* are the commercial adsorbents from the work of Ribeiro et al.[16]

Figure 12. For a layered bed of the commercial activated carbon and UiO-66(Zr)-Br: 1 ppm breakthrough time for CO_2 at the end of the activated layer (open spheres) and the N_2 breakthrough time at the end of the column (filled spheres). The grey shaded region in the graph denotes the PSA cycle durations for which both operating conditions are satisfied: N_2 retention inside the column and CO_2 retention in the activated carbon layer.

For Table of Contents Only

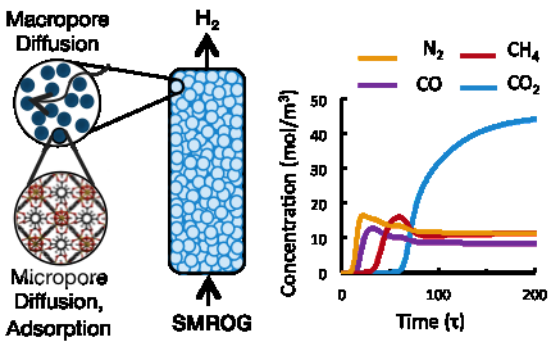

A multi-scale study of MOFs as adsorbents in H_2 PSA purification

*Ana-Maria Banu, Daniel Friedrich, Stefano Brandani, Tina Düren**

Institute for Materials and Processes, School of Engineering, The University of Edinburgh,

Sanderson Building, The King's Buildings, Mayfield Road

Edinburgh, EH9 3JL, UK

SUPPORTING INFORMATION

1. Macropore and Micropore Diffusion Parameters

The linear driving force (LDF) parameters describing macropore and micropore diffusion are given in **Table S 1**. Micropore diffusivities were calculated using NEMD simulations, and the average microporous particle (crystallite) radius was assumed to be 3 μm. Macropore diffusivities were calculated by using the Chapman-Enskog equation for binary mixtures

$$D_{ij} = 0.0018583\sqrt{\frac{1}{M_i}+\frac{1}{M_j}}\left(\frac{1}{\sigma_{ij}^2}\right)\frac{T^{3/2}}{P\Omega_{ij}} \tag{1}$$

where M_i and M_j are the molar masses of each binary mixture component, and Ω_{ij} is the "collision integral" and is a function of k_BT/ε_{ij}. σ_{ij} is the separation distance between i and j at the lowest point of the Lennard-Jones potential well, while ε_{ij} is the energy at the lowest point of the well. The Ω_{ij} parameters were taken from the appendix tables of Bird et al..[1] The Chapman-Enskog equation was extended to the five-component mixture as follows:

$$D_{im} = \frac{1-X_i}{\sum_{j\neq i}^{n}\frac{X_j}{D_{ij}}} \tag{2}$$

Here X_i and X_j are the molar fractions of the components in the mixture. The macropore diffusivity can then be determined by dividing D_{im} by a tortuosity factor of $\tau = 2$.

$$D_p = \frac{D_{im}}{\tau} \tag{3}$$

The pellet radius of the commercial zeolite and activated carbon of Ribeiro et al. were 0.85 mm and 1.17 mm respectively. In this work the pellet radius for the four MOFs was set to be the same as that of the zeolite, that is 0.85 mm.

Table S 1. LDF coefficients used to describe diffusion through MOF pellet macropores and micropore

	D_c/r_c^2 (s^{-1})						D_p/r_p^2 (s^{-1}) MOFs, Zeolite*	D_p/r_p^2 (s^{-1}) AC*
	UiO-66(Zr)	**UiO-66(Zr)-Br**	**UiO-67(Zr)**	**Zr-Cl_2AzoBDC**	**Zeolite***	**AC***		
H_2	4.94E+03	1.20E+03	1.71E+04	2.14E+04	9.23E-02	8.89E-02	6.91	3.65
CO_2	5.87E+02	2.76E+02	2.96E+03	3.52E+03	1.87E-04	1.24E-02	4.75	2.51
CO	5.86E+02	4.89E+01	2.60E+03	3.84E+03	4.22E-03	2.11E-02	4.17	2.20
CH_4	8.19E+02	2.34E+01	3.68E+03	3.12E+03	1.04E-02	3.96E-02	4.24	2.24
N_2	4.54E+02	2.62E+01	2.53E+03	3.19E+03	2.13E-02	2.29E-02	4.18	2.21

Note: The large difference between the D_c/r_c^2 values calculated for the four MOFs and those provided by Ribeiro et al. for Zeolite* and AC* may be in part due a difference in the r_c values used here and in the calculations of Ribeiro and coworkers.[2] It must be mentioned however, that the transport diffusivities of molecules through structures containing pores in the range of 4 to 10 Å can vary by several orders of magnitude as shown by Ruthven and Post[3], depending on the chemistry and topology of the materials.

2. EF-NEMD Calculation Details

The Onsager method is used in order to relate the flux to the chemical potential gradient

$$J = -L\nabla\mu \tag{4}$$

where L is sometimes referred to as an Onsager coefficient. The transport diffusion coefficient D_t is related to L as follows:

$$D_t = L\Gamma \quad \text{where} \quad \Gamma = \frac{RT}{c}\frac{d\ln f}{d\ln c} \tag{5}$$

The d*(*ln *f)/*d*(*ln *c)* term is also known as the thermodynamic correction factor and can be determined directly from the single component adsorption isotherm. For a dual site Langmuir isotherm expression the thermodynamic correction factor becomes[4]:

$$\Gamma = \frac{1}{\left[\frac{q_i^1}{q_i}\left(1-\frac{q_i^1}{q_{i,s}^1}\right)+\frac{q_i^2}{q_i}\left(1-\frac{q_i^2}{q_{i,s}^2}\right)\right]} \tag{6}$$

Here $q_i^{\,1}$ and $q_i^{\,2}$ are used to denote the loadings at each of the two sites at a given pressure, and $q_{i,s}^{\,1}$ and $q_{i,s}^{\,2}$ are the saturation loadings. In order to determine the Onsager coefficients for each of our adsorbates, external force non-equilibrium molecular dynamics (EF-NEMD) simulations were carried out. [5] In EF-NEMD, an external force is applied to the adsorbate molecules inside the framework pores in order to imitate a chemical potential gradient effect. This results in a movement of molecules along the direction of the applied force, and the molecular flux can be measured. Here a force was applied along the x-direction.

The flux was then calculated using

$$\langle J \rangle = \frac{1}{V\tau_{sim}}\left\langle \sum_{k=1}^{N}\left[r_k(t) - r_k(0)\right]\right\rangle \tag{7}$$

where r_k refers to the position of molecule k along the direction in which the force was applied, V represents the unit cell volume and τ is the time span of the simulation. The sum of the molecular displacements at each time point is also known as the displacement correlation function (DCF). Finally, the Onsager coefficients were determined using

$$L = \frac{\langle J \rangle}{F} \tag{8}$$

and used in calculating the transport diffusion coefficients for each of the adsorbates. It should be noted that this simple model applies only to the single component diffusion case.

3. Breakthrough Simulation Details

The mass balances along the column for axial dispersed plug flow and the linear driving force model used to represent the equivalent diffusion through both, the macropores and the micropores (bi-LDF), are given by

$$\frac{\partial c_i}{\partial t} + \frac{(1-\varepsilon)}{\varepsilon} \cdot \frac{\partial Q_i}{\partial t} + \frac{\partial (c_i \cdot v)}{\partial z} + \frac{\partial J_i}{\partial z} = 0$$

$$Q_i = \varepsilon_p c_i^m + (1-\varepsilon_p) q_i$$

$$\varepsilon_p \frac{dc_i^m}{dt} + (1-\varepsilon_p) \frac{dq_i}{dt} = k_i^p \frac{A_p}{V_p} (c_i - c_i^m),$$

$$\frac{dq_i}{dt} = k_i^{cr} \frac{3}{r_c} (q_i^* - q_i)$$

Here i goes from 1 to the number of components N_c. The value of the adsorbate concentration at equilibrium q_i^* depends on the dual-site, multi-component Langmuir isotherm

$$q_i^* = \frac{q_{i,s}^1 b_i^1 \exp\left(\frac{-\Delta \widetilde{H}_i^1}{RT}\right) P x_i}{1 + \sum_{j=1}^{N_c} b_j^1 \exp\left(\frac{-\Delta \widetilde{H}_i^1}{RT}\right) P x_j} + \frac{q_{i,s}^2 b_i^2 \exp\left(\frac{-\Delta \widetilde{H}_i^2}{RT}\right) P x_i}{1 + \sum_{j=1}^{N_c} b_j^2 \exp\left(\frac{-\Delta \widetilde{H}_i^2}{RT}\right) P x_j}$$

The energy balance in the column is written in terms of the internal energy in the fluid and solid phase plus an equation for the wall temperature

$$\varepsilon \frac{\partial U_f}{\partial t} + (1-\varepsilon)\frac{\partial U_p}{\partial t} + \varepsilon \frac{\partial (H_f \cdot u)}{\partial z} + \frac{\partial J_T}{\partial z} + \sum_{i=1}^{N_c} \frac{\partial (J_i \tilde{H}_i)}{\partial z} + h_w \frac{A_c}{V_c}(T_f - T_w) = 0$$

$$\frac{dU_p}{dt} = \varepsilon_P \frac{dU_{p,f}}{dt} + (1-\varepsilon_P)\frac{dU_{p,s}}{dt} = h \frac{A_p}{V_p}(T_f - T_p)$$

$$\rho_w c_{P,w} \frac{dT_w}{dt} + h_w \frac{A_c}{V_w}(T_w - T_f) + U\alpha_{wl}(T_w - T_\infty) = 0$$

The diffusive flux of component *i* in the fluid phase J_i, the thermal diffusive flux J_T and the logarithmic mean surface to volume ratio of the column wall are given by

$$J_i = -D_L c_T \frac{\partial x_i}{\partial z}$$

$$J_T = -\lambda_L \frac{\partial T_f}{\partial z}$$

$$\alpha_{wl} = \frac{1}{(2R_c + \delta)\ln\left(\frac{2R_c + \delta}{2R_c}\right)}$$

Here the axial dispersion coefficient is given by D_L, the axial thermal conductivity by λ_L and the column wall thickness by δ. The component mole fractions are given by x_i.

The interstitial flow velocity *v* is calculated from the Ergun equation

$$-\frac{\partial P}{\partial z} = \frac{150\mu(1-\varepsilon)^2}{(2R_p)^2 \varepsilon^2} v + \frac{1.75\rho_f (1-\varepsilon)}{2R_p \varepsilon} v|v|$$

The boundary equations for the mass and energy balance in the column are given by the Danckwert's boundary conditions which can be written as

$$J_T\big|_{z=0} = v(\breve{H}_{f,0-} - \breve{H}_{f,0})$$

$$J_T\big|_{z=L_c} = 0$$

$$J_i\big|_{z=0} = v(c_{i,0-} - c_{i,0})$$

$$J_i\big|_{z=L_c} = 0$$

where the superscript indicates the enthalpy or concentrations to the left of the column boundary, respectively.

The constitutive equations for the energy balance are given by

$$U_f = U_{ref} + \int_{T_{ref}}^{T} c_T \widetilde{c}_V dT'$$

$$H_f = H_{ref} + \int_{T_{ref}}^{T} c_T \widetilde{c}_P dT'$$

$$U_p = \varepsilon_p U_{p,f} + \left(1 - \varepsilon_p\right) U_{p,s}$$

$$U_{p,f} = U_{p,ref} + \int_{T_{ref}}^{T} c_T^m \widetilde{c}_V dT'$$

$$U_{p,s} = U_{sol} + U_{ads}$$

$$U_{sol} = U_{sol,ref} + \int_{T_{ref}}^{T_P} \rho_s c_{P,sol} dT'$$

$$U_{ads} = H_{ads} = H_{ads,ref} + \int_{T_{ref}}^{T_P} q_T \widetilde{c}_{P,ads} dT' - \left(-\Delta H_{ads}\right)_{T_p}$$

$$\left(-\Delta H_{ads}\right)_{T_p} = \sum_{i=1}^{N_C} \int_0^{q_i} \left(-\Delta H_i\right)_{T_p, q_{j \neq i}} dq_i'$$

$$\widetilde{H}_i = \widetilde{H}_{i,ref} + \int_{T_{ref}}^{T} \widetilde{c}_{P,i} dT'$$

U_{sol} and U_{ads} are the internal energy per unit volume in the adsorbent and the adsorbate, respectively. The subscript 'ref' indicates the reference value at T_{ref} and P_{ref}. The total concentration in the fluid phase and in the macropore are given by c_T and c_T^m, respectively. ρ_s is the solid crystal density, q_T is the total adsorbed concentration in the micropore and $c_{P,sol}$ is the specific heat capacity at constant pressure in the solid phase.

The molar heat capacities at constant volume $\widetilde{c}_V$ in the fluid phase and at constant pressure in the fluid phase $\widetilde{c}_P$ and in the adsorbed phase $\widetilde{c}_{P,ads}$ are calculated from the respective component heat capacities in the following way

$$\widetilde{c}_V = \sum_{i=1}^{N_c} x_i \widetilde{c}_{V,i}$$

$$\widetilde{c}_P = \sum_{i=1}^{N_c} x_i \widetilde{c}_{P,i}$$

$$\widetilde{c}_{P,ads} = \sum_{i=1}^{N_c} \frac{q_i}{q_T} \widetilde{c}_{P,i}$$

The parameters used to describe the PSA column and the adsorbent materials modeled in the breakthrough simulations are give in Table S 2.

Table S 2. Column parameters and properties of adsorbents used in this work, which were taken from the work of Ribeiro et al. [2, 6]

Feed flow rate (adsorption) (Nm^3/h)	12.2
Purge gas flow rate (desorption (Nm^3/h)	5.0
Inlet pressure (bar)	7
Column length (m)	1
Column diameter (m)	0.2
Wall density (kg/m^3)	8238
Wall specific heat (J/kg/K)	500
Void fraction of bed	0.38
Void fraction of pellet	0.25
Particle radius (m)	Activated carbons: 1.17×10^{-3} MOFs and zeolites : 0.85×10^{-3}
Heat transfer coefficient pellet-bed ($J/m^2/s/K$)	219
Heat transfer coefficient column wall ($J/m^2/s/K$)	94
Particle specific heat capacity (J/kg/K)	Activated carbons: 709 MOFs and zeolites: 920

4. Dual Site Langmuir Model Parameters

Table S 3. Dual Site Langmuir Parameters for the four MOFs

UiO-67(Zr)

Adsorbate	q^1_s mol/m^3	b^1 bar^{-1}	q^2_s mol/m^3	b^2 bar^{-1}	$-\Delta H_{ads}$ kJ/mol
H_2	6346.78	4.88E-09	9383.60	6.16E-04	5.013
CO_2	6346.78	5.27E-05	9383.60	3.16E-05	20.37
CO	6346.78	1.39E-04	9383.60	1.54E-04	11.87
CH_4	6346.78	2.95E-05	9383.60	2.00E-04	14.17
N_2	6346.78	3.77E-05	9383.60	2.62E-04	10.69

Zr-Cl_2AzoBDC

Adsorbate	q^1_s mol/m^3	b^1 bar^{-1}	q^2_s mol/m^3	b^2 bar^{-1}	$-\Delta H_{ads}$ kJ/mol
H_2	6191.68	1.02E-14	11857.38	5.72E-04	4.69
CO_2	6191.68	6.17E-05	11857.38	5.91E-05	17.28
CO	6191.68	4.47E-05	11857.38	1.58E-04	11.31
CH_4	6191.68	9.59E-06	11857.38	1.34E-04	13.51
N_2	6191.68	1.19E-06	11857.38	1.94E-04	10.37

UiO-66(Zr)

Adsorbate	q^1_s mol/m^3	b^1 bar^{-1}	q^2_s mol/m^3	b^2 bar^{-1}	$-\Delta H_{ads}$ kJ/mol
H_2	4620.80	2.79E-04	5028.37	2.79E-04	6.75
CO_2	4620.80	2.78E-06	5028.37	3.15E-05	26.54
CO	4620.80	1.33E-05	5028.37	1.48E-04	15.89
CH_4	4620.80	1.18E-04	5028.37	1.67E-05	18.60
N_2	4620.80	1.94E-04	5028.37	1.42E-05	14.62

UiO-66(Zr)-Br

Adsorbate	q^1_s mol/m^3	b^1 bar^{-1}	q^2_s mol/m^3	b^2 bar^{-1}	$-\Delta H_{ads}$ kJ/mol
H_2	3460.93	2.30E-04	4618.56	2.28E-04	7.46
CO_2	3460.93	6.85E-07	4618.56	2.47E-05	29.67
CO	3460.93	1.48E-04	4618.56	7.99E-06	18.22
CH_4	3460.93	1.37E-04	4618.56	3.15E-06	21.00
N_2	3460.93	1.59E-04	4618.56	6.29E-06	16.69

Table S 4. Dual Site Langmuir parameters for AC* and Zeolite*, the commercial adsorbents from the work of Ribeiro et al. [2]

AC*					
Adsorbate	q^1_s	b^1	q^2_s	b^2	$-\Delta H_{ads}$
	mol/m^3	bar^{-1}	mol/m^3	bar^{-1}	kJ/mol
H_2	811.85	3.38E-05	3785.52	3.39E-05	12.80
CO_2	811.85	4.65E-05	3785.52	3.35E-06	29.10
CO	811.85	1.56E-05	3785.52	9.59E-06	22.60
CH_4	811.85	2.21E-04	3785.52	8.92E-06	22.70
N_2	811.85	4.91E-04	3785.52	2.13E-05	16.30
Zeolite*					
Adsorbate	q^1_s	b^1	q^2_s	b^2	$-\Delta H_{ads}$
	mol/m^3	bar^{-1}	mol/m^3	bar^{-1}	kJ/mol
H_2	3888.07	1.07E-06	950.34	5.36E-04	9.23
CO_2	3888.07	2.43E-05	950.34	3.72E-07	36.00
CO	3888.07	5.87E-07	950.34	2.12E-05	29.80
CH_4	3888.07	2.08E-05	950.34	1.30E-04	20.60
N_2	3888.07	8.99E-06	950.34	1.14E-04	20.40

Table S 5. Dual Site Langmuir parameters for Calgon PCB and Single Site Langmuir parameters for Zeolite 5A[7]. Note that in reference 6 the heats of adsorption were reported with the wrong units. We have confirmed with the authors that the values and units provided here are correct.

Calgon PCB					
Adsorbate	q^1_s	b^1	q^2_s	b^2	$-\Delta H_{ads}$
	mol/m^3	bar^{-1}	mol/m^3	bar^{-1}	kJ/mol
H_2	5950.97	1.59E-03	1201.00	1.59E-03	12.06
CO_2	5950.97	4.61E-02	1201.00	3.57E-03	21.93
CO	5950.97	1.33E-02	1201.00	6.33E-08	18.00
CH_4	5950.97	3.04E-02	1201.00	8.23E-05	17.96
N_2	5950.97	2.39E-07	1201.00	8.33E-02	6.95
Zeolite 5A					
Adsorbate	q_s	b	$-\Delta H_{ads}$		
	mol/m^3	bar^{-1}	kJ/mol		
H_2	2594.04	5.32E-03	11.72		
CO_2	5089.04	2.86E+00	39.05		
CO	2799.63	2.79E-02	22.18		
CH_4	2589.98	1.95E-02	22.60		
N_2	3066.76	1.10E-02	22.90		

5. Validation of Breakthrough Simulations

The in-house PSA model was first validated by carrying out breakthrough simulations set up to reproduce experimental data.[8] In the work of Lopes et al, five multi component mixtures were fed through a column containing a commercial activated carbon, and the outlet concentrations were measured using a gas chromatograph. The inlet pressure was 5 bar, and a feed flow rate of 5 x 10^{-5} m^3/s was applied. The simulated breakthrough curves obtained using a mathematical model were in excellent agreement with the experimental data.[8] Here, the CySim software was used together with the modelling parameters of Lopes et al, in order to calculate the breakthrough behaviour for cases 1 and 5. The inlet stream of experiment 1 contains 70% H_2 and 30% CO_2 while experiment 2 involved a five component mixture made up 73:23:2.1:1.2:0.7 H_2:CO_2:CH_4:CO:N_2. In Figure S **1** the simulated breakthrough curves obtained in this study are plotted along with the experimental data of Lopes et al. Excellent agreement is observed for both mixtures considered, thereby confirming that the PSA simulator employed is able to accurately predict the breakthrough behaviour of mixtures of up to 5 components.

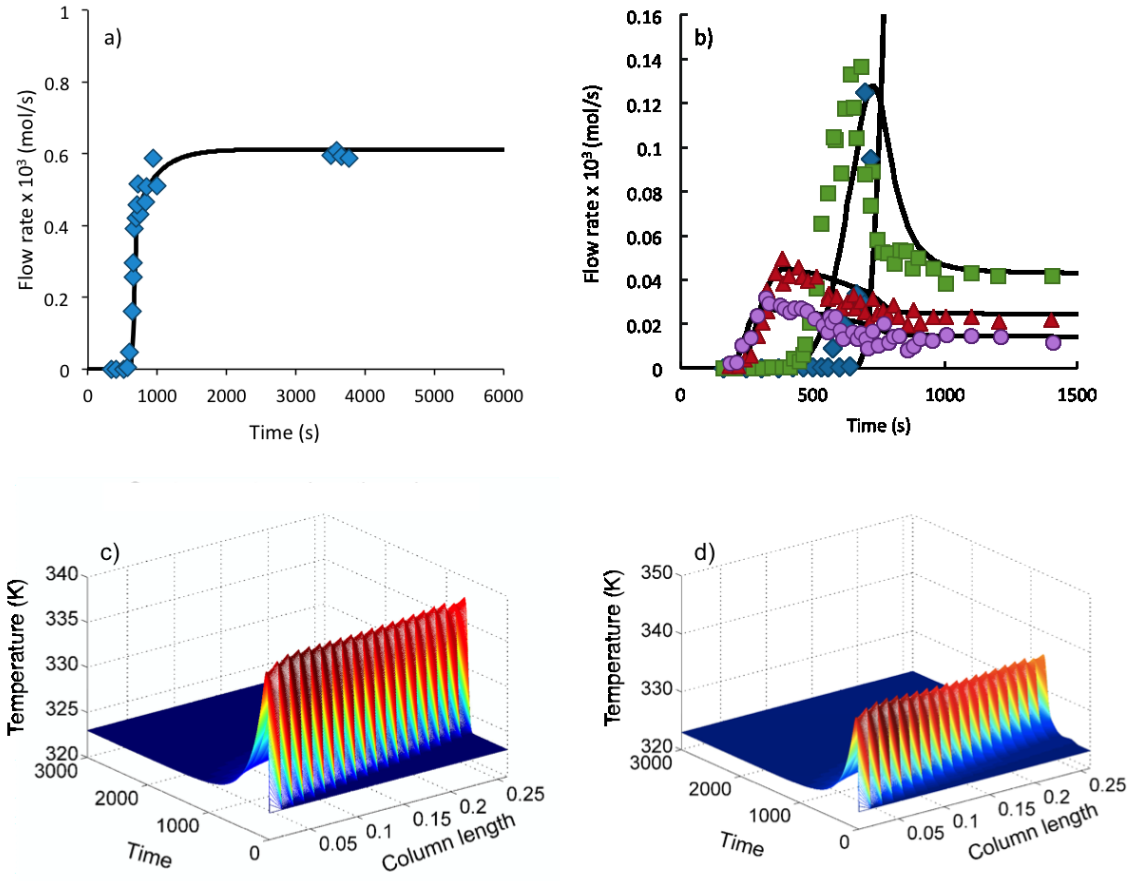

Figure S 1. Breakthrough curves for a) Case 1 and b) Case 5 of Lopes et al.[8], and gas temperature within the bed for c) Case 1 and b) Case 5. Case 1: 70% H_2, 30% CO_2.Case 5: 73% H_2, 23% CO_2, 2.1% CH_4, 1.2% CO, 0.7% N_2. Simulated breakthrough curves are shown as black lines, while experimental data is shown using symbols: blue diamonds CO_2, yellow spheres H_2, green squares CH_4, red triangles CO, purple spheres N_2. H_2 was omitted for clarity.

6. Validation of Adsorption Isotherms

The simulated isotherms for CO_2 and CH_4 adsorption in UiO-66(Zr) were compared to the experimental data presented by Yang et al.[9] as shown in **Figure S 2**. The simulated isotherms are in good agreement with the experimental isotherms. Additional validation studies could not be carried out for the remaining MOFs due to the unavailability of experimental data.

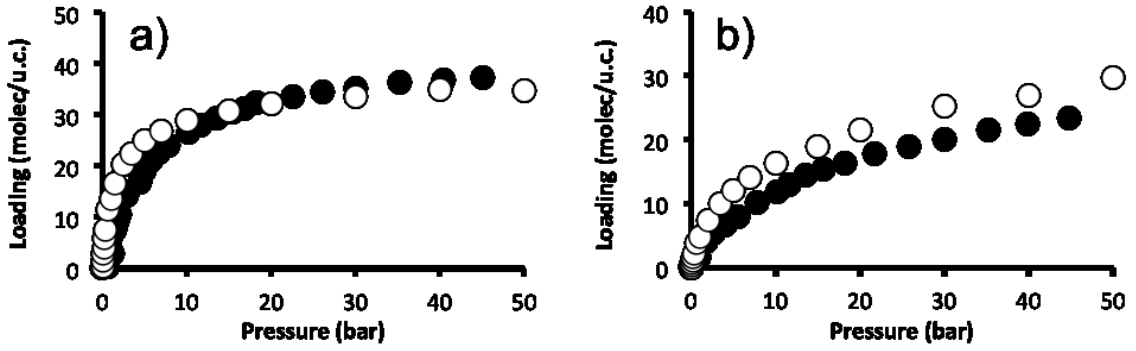

Figure S 2. Dehydroxylated UiO-66(Zr) adsorption isotherms for a) CO_2 and b) CH_4 from simulations (open spheres) and experiment (closed spheres). The experimental data is taken from the work of Yang et al.[9]

7. Working Capacities Equivalent to SMROG Composition

Working capacities were determined for each impurity at pressures corresponding to its partial pressure in an SMROG stream. Two operating ranges were considered: 1 – 7 bar given in Figure S 3, and 1 – 20 bar given in Figure S 4.

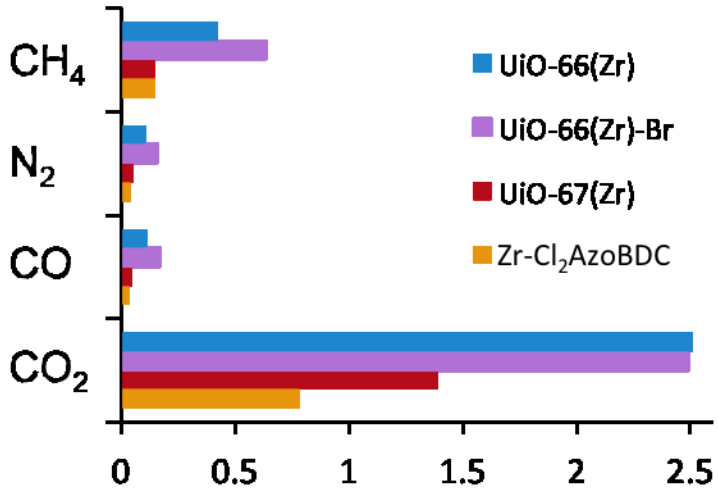

Figure S 3. Working capacities determined from binary adsorption data for pressure ranges resulting in equivalent SMROG impurity partial pressures in the 1 – 7 bar range.

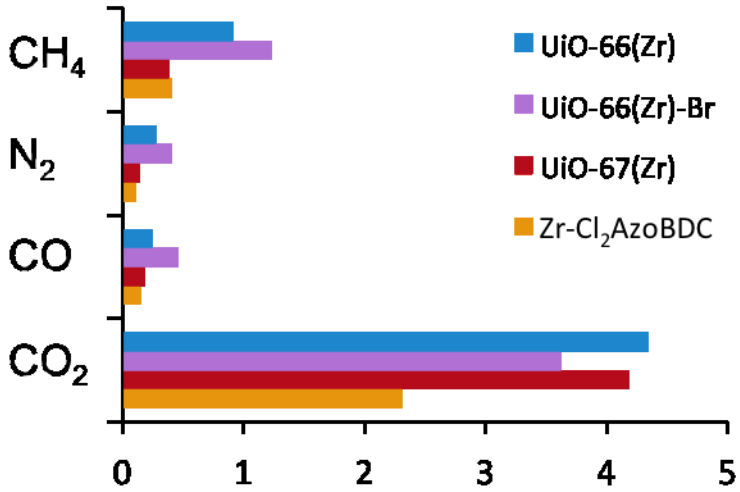

Figure S 4. Working capacities determined from binary adsorption data for pressure ranges resulting in equivalent SMROG impurity partial pressures in the 1 – 20 bar range.

The total binary mixture pressures resulting in impurity partial pressures equivalent to those in an SMROG stream at 1, 7 and 20 bar are given in **Table S 6**.

Table S 6. Impurity partial pressures in SMROG stream at 1, 7 and 20 bar.

	Binary Mixture Total Pressure (bar)			
P	**CO/H_2**	**CH_4/H_2**	**N_2/H_2**	**CO_2/H_2**
1 bar	0.1 (0.03/0.07)	0.13 (0.04/0.09)	0.13 (0.04/0.09)	0.53 (0.16/0.37)
7 bar	0.7 (0.21/0.49)	0.93 (0.28/0.65)	0.93 (0.28/0.65)	3.73 (1.12/2.61)
20 bar	2 (0.6/1.4)	2.67 (0.8/1.87)	26.7 (0.8/1.87)	10.7 (3.2/7.5)

8. Isosteric Heats of Adsorption

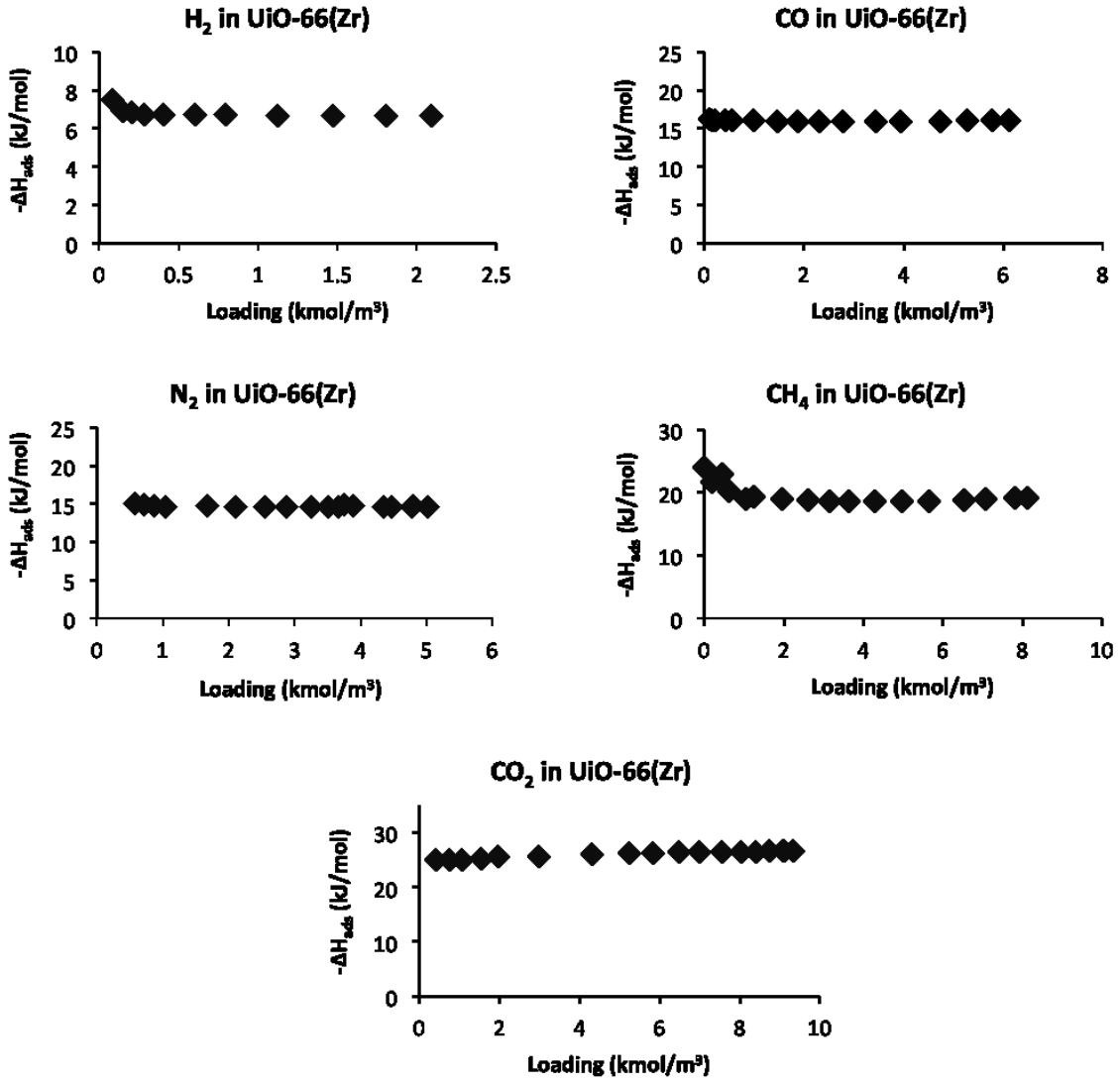

Figure S 5. Isosteric Heats of Adsorption for H_2, CO, N_2, CH_4 and CO_2 in UiO-66(Zr) at 303 K.

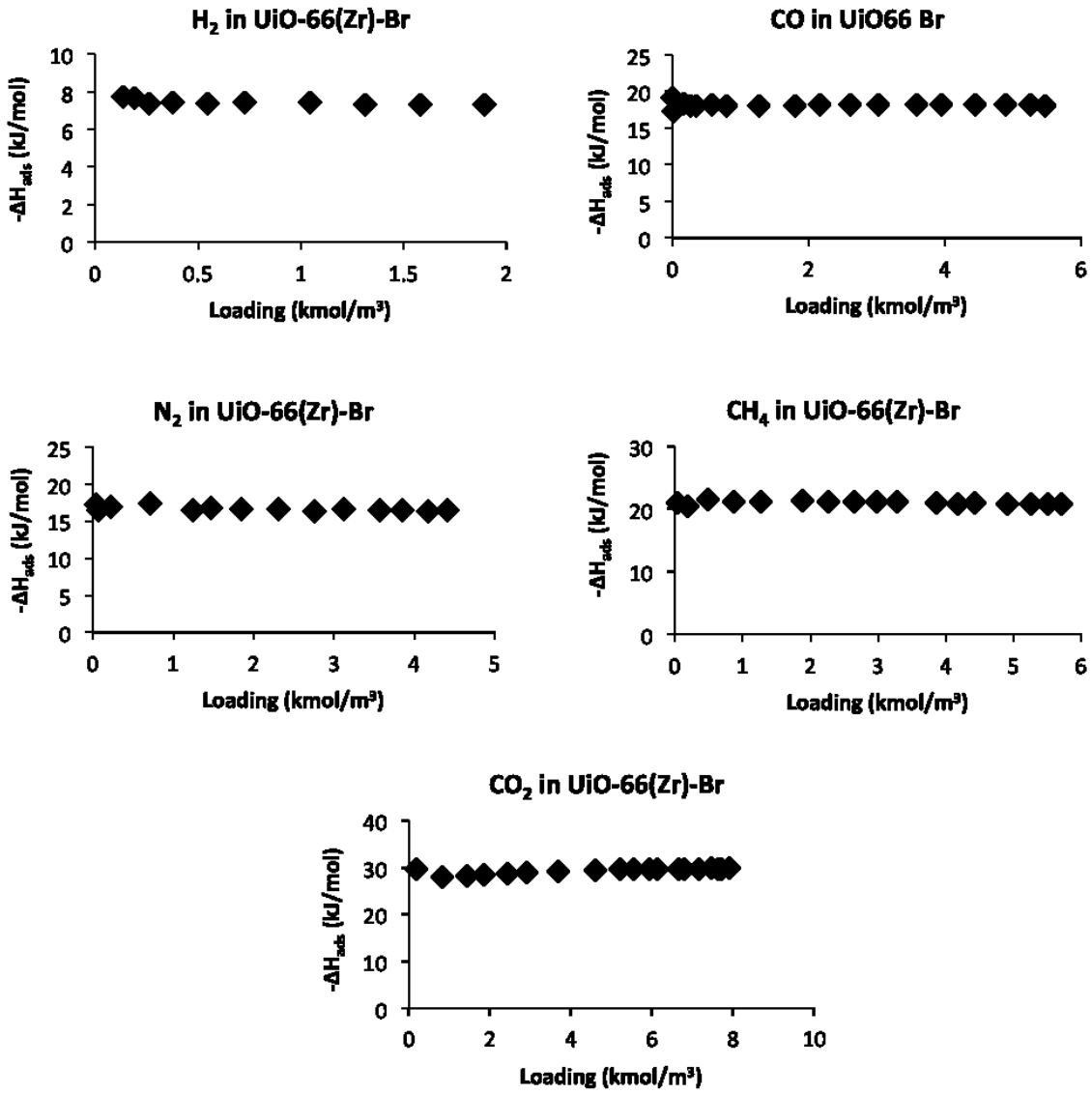

Figure S 6. Isosteric Heats of Adsorption for H_2, CO, N_2, CH_4 and CO_2 in UiO-66(Zr)-Br at 303 K.

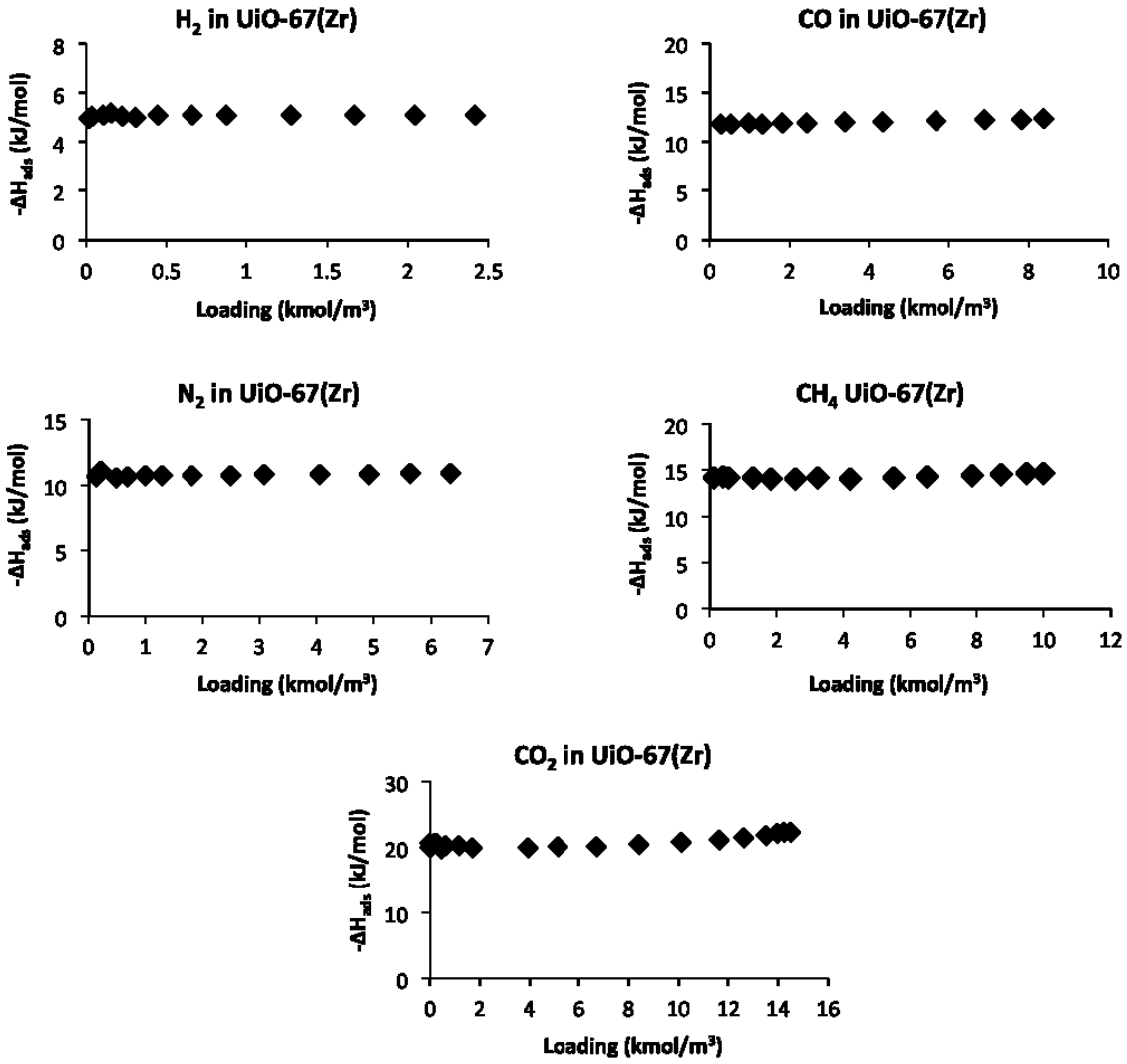

Figure S 7. Isosteric Heats of Adsorption for H_2, CO, N_2, CH_4 and CO_2 in UiO-67(Zr) at 303 K.

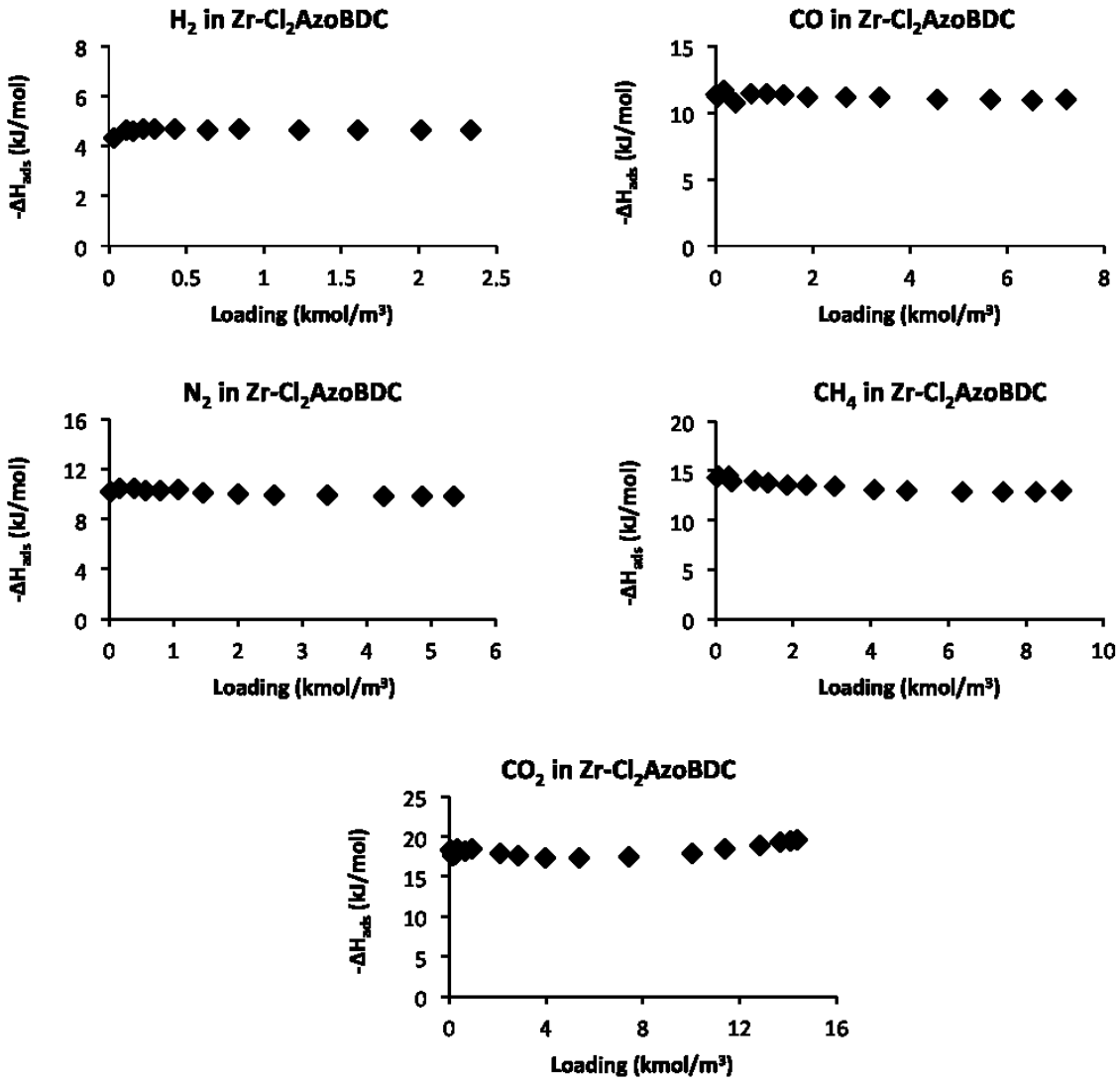

Figure S 8. Isosteric Heats of Adsorption for H_2, CO, N_2, CH_4 and CO_2 in Zr-Cl_2AzoBDC at 303 K.

9. Estimation of Bulk Densities

Table S 7. Estimated Bulk Densities based on the assigned pellet void fraction of 0.25 and bed void fraction of 0.38.

MOF	Crystal Density (kg/m3)	Pellet Density (kg/m3)	Bulk Density (kg/m3)
UiO-66(Zr)	1219	914	567
UiO-66(Zr)-Br	1597	1198	743
UiO-67	710	533	330
Zr-Cl_2AzoBDC	671	503	312

Nomenclature

A_c Internal column surface area, m^2

A_p Pellet surface area, m^2

b_i^j Adsorption equilibrium constant of site j for comp. i, Pa^{-1}

c_i Gas concentration of component i, mol m^{-3}

c_i^m Gas concentration of component i in the macropore, mol m^{-3}

c_T The total concentration in the fluid phase, mol m^{-3}

c_T^m The total concentration in the macropore, mol m^{-3}

$c_{P,sol}$ The specific heat capacity at constant pressure in the solid phase, J kg^{-1} K^{-1}

$c_{P,w}$ Specific heat capacity of the column wall, J kg^{-1} K^{-1}

$\widetilde{c}_P$ Molar heat capacity at constant pressure in the fluid phase, J mol^{-1} K^{-1}

$\widetilde{c}_{P,ads}$ Molar heat capacity at constant pressure in the adsorbed phase, J mol^{-1} K^{-1}

$\widetilde{c}_V$ Molar heat capacity at constant volume in the fluid phase, J mol^{-1} K^{-1}

D_c Micropore diffusivity, m^2s^{-1}

D_{ij} Macropore diffusivity for binary mixtures, cm^2 s^{-1}

D_{im} Macropore diffusivity for mixtures of more than two gases, cm^2 s^{-1}

D_p Macropore diffusivity, m^2s^{-1}

D_t Transport diffusivity, m^2s^{-1}

J Flux of molecules through micropores, mol m^{-2} s^{-1}

h Heat transfer coefficient between the pellet and the bed, W m^{-2} K^{-1}

h_w Heat transfer coefficient at the column wall, W m^{-2} K^{-1}

H_{ad} Dimensionless Henry's constant

H_f Enthalpy in the fluid phase per unit volume, J m^{-3}

$\widetilde{H}_i$ Partial molar enthalpy in the fluid phase of comp.i, J mol^{-1}

$\Delta\widetilde{H}_i^j$ Heat of adsorption of site j for comp.i, J mol^{-1}

J_i Diffusive flux of component i, mol m^{-2} s^{-1}

J_T Thermal diffusive flux, W m^{-2}

k_B Boltmann constant, J mol^{-1} K^{-1}

k_i^p LDF mass transfer coefficient of component i in the pellet, m s^{-1}

k_i^{cr} LDF mass transfer coefficient of component i in the crystal, m s^{-1}

L_c Column length, m

L Onsager coefficient, mol m^{-1} s^{-1}

M_i Molar mass of binary mixture component i, g mol^{-1}

P Pressure, Pa

P_{ref} Reference pressure, Pa

q_i Average adsorbed concentration of component i in the crystal, mol m^{-3}

q_i^* Adsorbed concentration of component iat equilibrium, mol m^{-3}

$q_{i,s}^j$ Saturation capacity of site j for comp. i, mol m^{-3}

q_T The total adsorbed concentration in the micropore, mol m^{-3}

Q_i Average adsorbed concentration of component i in the pellet, mol m^{-3}

r_k Position of molecule k, m

r_c Crystal radius, m

r_p Pellet radius, m

t Time, s

T_f Fluid temperature, K

T_{ref} Reference temperature, K

T_p Pellet temperature, K

T_w Column wall temperature, K

T_∞ Outside temperature, K

u Velocity, m s^{-1}

U External heat transfer coefficient, W m^{-2} K^{-1}

U_f Internal energy in the fluid phase per unit volume, J m^{-3}

U_p Internal energy in the pellet per unit volume, J m^{-3}

$U_{p,f}$ Internal energy in the macropore per unit volume, J m^{-3}

$U_{p,s}$ Internal energy in the solid phase per unit volume, J m^{-3}

U_{sol} internal energy per unit volume in the adsorbent, J m^{-3}

U_{ads} Internal energy per unit in the adsorbate, J m^{-3}

V Unit cell volume, m^3

v Interstitial flow velocity, m s^{-1}

V_c Column volume, m^3

V_p Pellet volume, m^3

V_w Column wall volume, m^3

X_i Molar fraction of component i in mixture of gases

X_i Molar fraction of component i in mixture of gases

z Spatial dimension, m

α_{wl} Mean surface area to volume ratio of the column wall, m^{-1}

δ Column wall thickness, m

ε Bed void fraction

ε_{ij} Interaction energy between molecules i and j at the lowest point on the Lennard-Jones potential well, J mol^{-1}

ε_p Pellet void fraction

λ_L Axial thermal conductivity and the column wall thickness, J m^{-1} s^{-1} K^{-1}

Γ Thermodynamic correction factor

$\Delta\mu$ Chemical potential gradient, J mol^{-1}

μ Viscosity, Pa s

Ω_{ij} Collision integral for the Chapman-Enskog diffusivity definition

ρ_f Fluid density, kg m^{-3}

ρ_s Solid density, kg m^{-3}

ρ_w Column wall density, kg m^{-3}

σ_{ij} Separation distance between molecules i and j at the lowest point on the Lennard-Jones potential well, Å

τ_{sim} Time span of NEMD simulation, s

τ Tortuosity factor

References

(1) Bird, R. B.; Stewart, W. E.; Lightfoot, E. N. *Transport Phenomena*. second ed.; Wiley International: Singapore, 2002.

(2) Ribeiro, A. M.; Grande, C. A.; Lopes, F. V. S.; Loureiro, J. M.; Rodrigues, A. E. A parametric study of layered bed PSA for hydrogen purification. *Chem. Eng. Sci.* **2008,** *63*, 5258.

(3) Ruthven, D. M.; Post, M. F. M. Diffusion in Zeolite Molecular Sieves. In *Introduction to Zeolite Science and Practice*, van Bekkum, H.; Jacobs, P. A.; Flannigen, E. M.; Jansen, J. C., Eds. Elsevier: Amsterdam, 1991; Vol. 58.

(4) Skoulidas, A. I.; Sholl, D. S.; Krishna, R. Correlation effects in diffusion of CH_4/CF_4 mixtures in MFI zeolite. A study linking MD simulations with the Maxwell-Stefan formulation. *Langmuir* **2003,** *19*, 7977.

(5) Maginn, E. J.; Bell, A. T.; Theodorou, D. N. Transport Diffusivity of Methane in Silicalite from Equilibrium and Nonequilibrium Simulations. *J. Phys. Chem.* **1993,** *97*, 4173.

(6) Mu, B.; Walton, K. S. Thermal Analysis and Heat Capacity Study of Metal–Organic Frameworks. *J. Phys. Chem. C* **2011,** *115*, 22748.

(7) Ahn, S.; You, Y.-W.; Lee, D.-G.; Kim, K.-H.; Oh, M.; Lee, C.-H. Layered two- and four-bed PSA processes for H_2 recovery from coal gas. *Chem. Eng. Sci.* **2012,** *68*, 413.

(8) Lopes, F. V. S.; Grande, C. A.; Rodrigues, A. E. Activated carbon for hydrogen purification by pressure swing adsorption: Multicomponent breakthrough curves and PSA performance. *Chem. Eng. Sci.* **2011,** *66*, 303.

(9) Yang, Q.; Wiersum, A. D.; Jobic, H.; Guillerm, V.; Serre, C.; Llewellyn, P. L.; Maurin, G. Understanding the Thermodynamic and Kinetic Behavior of the CO_2/CH_4 Gas Mixture within the Porous Zirconium Terephthalate UiO-66(Zr): A Joint Experimental and Modeling Approach. *J. Phys. Chem. C* **2011,** *115*, 13768.